NTNU
Norwegian University of Science and Technology

Institute of Petroleum Technology and Applied Geophysics

MASTER'S THESIS

FOR

STUD.TECHN. Asbjørn L. Johansen

FACULTY OF ENGINEERING SCIENCE AND TECHNOLOGY

NTNU

Date due: June 15, 2007 *New date due: August 31, 2007*

Discipline: Seismic

Title: "Time-lapse interferometric imaging using an active source"

Purpose of the work: Produce a synthetic seismic time-lapse dataset, and implement an interferometric method for imaging of the modelled time-lapse response.

This diploma thesis is to be carried out at the Department of Petroleum Technology and Applied Geophysics under guidance of Professor Martin Landrø.

Trondheim, January 22, 2006.

Jon Kleppe Instituttleder Dept. of Petroleum Technology	Martin Landrø Professor Dept. of Applied Geophysics

For Marie.

Abstract

The purpose of time-lapse seismic processing is to relate changes in seismic signals to changes in reservoir parameters. A synthetic time-lapse experiment has been conducted in order to provide a controlled test environment for an interferometric imaging algorithm. The time-lapse contrast is created by introducing a 51% increase in water saturation to a model by Gassmann fluid substitution.

A time-convolution algorithm was then applied on the dataset to verify the pre-processing steps, prior to applying the interferometric method. This method was also used to recursively remove time-lapse responses from the output data.

The time-convolution method has been successful in recursively removing the time-lapse responses as it passes through the contrast in the media, leaving only the difference reflections below.

It was found that the interferometric method responds well to the contrast of the reservoir, and shows a trend in accordance with expectations from the theory.

Preface

This thesis was written at the Norwegian University of Science and Technology in co-operation with SINTEF Petroleum Research. It is the continuation of a project work carried out during the autumn of 2006.

I would like to thank Menno Dillen[1] for his guidance and valuable discussions. His comments have greatly aided my understanding of the subject. The rest of the staff at SINTEF Petroleum Research has also contributed with input and a good working environment.

I would also like to thank Professor Martin Landrø[2] for allowing me to proceed with my thesis at SINTEF Petroleum Research, and for providing good suggestions and conversations.

Finally I want to thank my family and friends for all their support and patience, especially towards the end. At last a special thanks to Nina Bull Eide for designing the front page.

Trondheim,
August 2007 *Asbjørn L. Johansen*

[1] Senior Research Scientist, Seismic Department, SINTEF Petroleum Research

[2] Department of Applied Geophysics, Norwegian University of Science and Technology

Contents

List of Figures

List of Tables

Chapter 1
Introduction

In order to get the maximum value from a field it is vital to have a reservoir model which is as accurate as possible in order to come up with an optimal drainage and injection strategy. Although a lot of data can be collected via instruments in the wells, this provides no information about the situation away from the well. Time-lapse seismic is therefore becoming an increasingly important tool for monitoring changes in hydrocarbon reservoirs due to production, and can provide valuable input to the reservoir model.

To provide useful input in a reservoir management setting, the change in the seismic signal must be attributed to a contrast in physical properties of the reservoir. This means that some inversion scheme is needed.

There are many challenges associated with the acquisition and processing of time-lapse seismic surveys. An important challenge is to achieving a high degree of repeatability of geometry between surveys. A low degree of repeatability can cause problems when attempting to produce difference measurements (Landrø, 1999; Landro et al., 1999). Highly heterogenous reservoirs and random noise also contribute to the uncertainty.

A promising method for imaging time-lapse data is the use of boundary interaction integrals to produce difference measurements from seismic data sets. Two such a methods are described in Dillen (2000). One uses a time-convolution approach to produce difference wave fields, while the other is based on a time-correlation approach to represent phase differences.

1.1 Motivation

Since both methods mentioned have been implemented and found to produce good results for one-dimensional problems, it is desirable to extend this to two-dimensional problems. For the time-convolution method this has also been demonstrated in Dillen (2000), so it will be a case of reproducing the

same results to verify that the processing scheme is correctly implemented and able to produce sensible output.

With the time-correlation method the goal is to demonstrate sensitivity to small variations in reservoir thickness in addition to velocity changes.

1.2 Notation

Throughout this thesis the three-dimensional space $\mathbb{R}^3$ is considered. Within this space a Cartesian reference frame is used to define three mutually perpendicular base vectors, $\{\boldsymbol{i}_1, \boldsymbol{i}_2, \boldsymbol{i}_3\}$, which form a right-handed system. The vector $\boldsymbol{x}$, specified by the Cartesian coordinates $\{x_1, x_2, x_3\}$ and written as $\boldsymbol{x} = (x_1, x_2, x_3)$, defines a position in space and is given by

$$\boldsymbol{x} = x_1\boldsymbol{i}_1 + x_2\boldsymbol{i}_2 + x_3\boldsymbol{i}_3. \tag{1.1}$$

To identify when the transverse coordinates $\{x_1, x_2\}$ are used, the positional vector is also denoted by $\boldsymbol{x} = (\boldsymbol{x}_T, x_3)$, with the transverse coordinate given by

$$\boldsymbol{x}_T = x_1\boldsymbol{i}_1 + x_2\boldsymbol{i}_2. \tag{1.2}$$

The Einstein summation convention is used, such that one can write

$$\boldsymbol{x} = x_i\boldsymbol{i}_i, \tag{1.3}$$

where a repeated lower-case Latin subscript takes the values $\{1, 2, 3\}$.

Time is given by the coordinate $\{t\}$ in the one-dimensional space $\mathbb{R}$, and denoted by t.

Give the wave field $f(\boldsymbol{x}, t)$, the Fourier transform of this wave field will decorated with a $\hat{}$, such that

$$f(\hat{\boldsymbol{x}}, \omega) = \int_{-\infty}^{\infty} f(\boldsymbol{x}, t)\mathrm{e}^{-\mathrm{i}\omega t}\mathrm{dt}, \tag{1.4}$$

with i being the imaginary unit, e the base of the natural logarithm, and ω denoting angular frequency.

$$\omega = 2\pi f \tag{1.5}$$

When using partial derivates these are given with respect to the variable given in subscript

$$\partial_t f(\boldsymbol{x}, t) = \frac{\partial}{\partial t} f(\boldsymbol{x}, t). \tag{1.6}$$

For derivatives with respect to vector arguments the Einstein summation convention is used, and the derivatives are given by

$$\partial_k f_k(\boldsymbol{x}, t) = \frac{\partial}{\partial_{\boldsymbol{x}_1}} f(\boldsymbol{x}, t) + \frac{\partial}{\partial_{\boldsymbol{x}_2}} f(\boldsymbol{x}, t) + \frac{\partial}{\partial_{\boldsymbol{x}_3}} f(\boldsymbol{x}, t). \tag{1.7}$$

Chapter 2
Theory

2.1 Fluid substitution

Fluid substitution is often carried out by applying the low-frequency Gassmann theory (Gassmann, 1951). The equations presented by Gassmann relate the saturated bulk modulus of a rock to it's porosity, the bulk modulus of the porous rock frame, the bulk modulus of the mineral matrix, and the bulk modulus of the pore fluids

$$K_{sat} = K_{fr} + \frac{(1 - \frac{K_{fr}}{K_{ma}})^2}{\frac{\phi}{K_{fl}} + \frac{1-\phi}{K_{ma}} - \frac{K_{fr}}{K_{ma}^2}}. \tag{2.1}$$

Here K_{sat} is the saturated bulk modulus, K_{ma} is the bulk modulus of the mineral matrix, K_{fl} is the bulk modulus of the pore fluids, K_{fr} is the bulk modulus of the porous rock frame, and ϕ is porosity.

There are two important assumptions for the application of Gassmann's equation. The first is that the rock is homogeneous and isotropic, and that the pore space is completely connected. The second restricts its use to low enough frequencies. This implies that the pore pressure must be equalised over a length scale much larger than the pore size and much less than the seismic wavelength (Smith et al., 2003).

An important point mentioned by Avseth et al. (2005, p. 19) is that a gas saturated rock should not be treated as a dry rock; the gas should be treated as a fluid when performing the fluid substitution.

The workflow for performing fluid substitution shown in this chapter, is the same as presented by Smith et al. (2003).

2.1.1 Basic relationships

To relate a rock's bulk modulus to pressure wave velocity, shear wave velocity and density the following relationship is used

$$K = \rho_B(V_p^2 - \frac{4}{3}V_s^2). \tag{2.2}$$

In this relationship ρ_B is the bulk density of the rock, V_p is the pressure wave velocity, and V_s the shear wave velocity. The equation can easily be solved for V_p, shown in Eq. (2.13).

The shear modulus of the rock is given by the following equation

$$G = \rho_B V_s^2. \tag{2.3}$$

This equation can be solved with respect to V_s, see Eq (2.14).

What is important to recognise from these relationships is that the saturated bulk modulus of a rock may be sensitive to the composition of the pore fluid, while the shear modulus is insensitive to pore fluid (Berryman, 1999).

The last basic equation for doing fluid substitution gives the relationship between the bulk density (ρ_B), the pore fluid density (ρ_{fl}), porosity (ϕ), and the rock matrix' grain density (ρ_{ma})

$$\rho_B = \rho_{ma}(1 - \phi) + \rho_{fl}\phi. \tag{2.4}$$

2.1.2 Rock and fluid properties

Before performing the actual fluid substitution the porosity of the rock (ϕ), properties of the pore fluids, the bulk modulus of the mineral matrix (K_{ma}), and the bulk modulus of the porous rock frame (K_{fr}) must be determined. All these parameters can be determined from laboratory measurements or wire-line logs.

The first step is to determine the porosity of the rock. By solving Eq. (2.4) for porosity it can be calculated from wire-line log values.

Prior to performing fluid substitution it is also necessary to know the properties of the in-situ pore fluids, as well for the fluids to be substituted into the rock.

There is usually more than one type of pore fluid, and it is therefore necessary to determine the properties of each fluid and then mix them according to some physical principle. An assumption of Gassmann's equation is that the pore space is completely connected and the fluid pressure is equilibrated throughout the pore space. Because of this and an assumption of a homogeneous fluid, uniformly distributed in the pore space, enables the calculation of the pore fluids bulk modulus by the Reuss average (Mavkov et al., 1998)

$$K_{fl} = \left(\sum_{i=1}^{N} \frac{S_i}{K_i}\right)^{-1}, \tag{2.5}$$

where K_{fl} is the bulk modulus of the mixed fluids and K_i and S_i is the bulk modulus and saturation of each fluid components respectively. For a simple two-component case with water and hydrocarbons this can be expanded as

$$K_{fl} = \left(\frac{S_w}{K_w} + \frac{1 - S_w}{K_{hc}} \right)^{-1}, \tag{2.6}$$

where S_w and K_w is the saturation and bulk modulus of the water respectively, and K_{hc} is the bulk modulus of the hydrocarbon component.

For the bulk density a simple mixture can be used

$$\rho_{fl} = \sum_{n=1}^{N} S_i \rho_i. \tag{2.7}$$

Again this is expanded for the simple case of water and hydrocarbons, resulting in

$$\rho_{fl} = S_w \rho_w + (1 - S_w)\rho_{hc}. \tag{2.8}$$

Here ρ_w and ρ_{hc} is the density of water and hydrocarbon. This equation can together with Equation (2.6) easily be expanded to include additional fluid components, as is often required when dealing with hydrocarbon reservoirs where there is typically three types of pore fluid present; formation water, oil and gas.

Next the properties of the mineral matrix has to be defined. This requires knowledge about the mineralogical composition of the rock. Such knowledge can be gained either through measurements on core plugs or estimated via wire-line logs. Which technique is required depends on the complexity of the lithology to be modelled.

Once the volumetric fraction of each component of the rock matrix is known, the bulk moduli (K_{ma}) can be determined by using e.g. Voight-Reuss-Hill averaging. In this technique the Voight average represents an upper boundary, while the Reuss average gives the lower boundary of the bulk modulus. The Voight-Reuss-Hill average is simply the average of these.

$$K_{Reuss} = \left(\frac{F_1}{K_1} + \frac{F_2}{K_2} \right)^{-1} \tag{2.9}$$

$$K_{Voight} = (F_1 K_1 + F_2 K_2) \tag{2.10}$$

$$K_{VRH} = \frac{1}{2} \left(K_{Ruess} + K_{Voight} \right) \tag{2.11}$$

In these equations F_1 and F_2 represent the volumetric fraction of each component, and K_1 and K_2 are the bulk moduli. Both Eqs. (2.9) and (2.10) can easily be expanded to include more than two components.

The last property to be determined is the bulk modulus of the porous rock framework, K_{fr}. Since this and the shear modulus (G) are properties of the framework and thus are not influenced by the fluid substitution, this calculation is only done once, and these parameters are later considered as constants.

There are several ways to determine K_{fr}, either from velocity measurements on core samples, by empirical relationships or from wire-line log data. When finding K_{fr} from wire-line data Eq. (2.1) is solved for K_{fr}

$$K_{fr} = \frac{K_{sat}\left(\frac{\phi K_{ma}}{K_{fl}} + 1 - \phi\right) - K_{ma}}{\frac{\phi K_{ma}}{Kfl} + \frac{K_{sat}}{K_{ma}} - 1 - \phi}. \tag{2.12}$$

The saturated bulk modulus (K_{sat}) for the in-situ rock is calculated by Eq. (2.2), and the remaining terms can then be calculated from the process described earlier.

2.1.3 Velocities

When porosity and properties of the rock frame and mineral matrix have been calculated it is possible to use Eq. (2.1) to determine the bulk modulus with any chosen pore fluids.

The next step is then to solve Eq. (2.2) with respect to V_p to find the new pressure wave velocity

$$V_p = \sqrt{\frac{K + \frac{4}{3}G}{\rho_B}}, \tag{2.13}$$

and Eq. (2.3) with respect to V_s so that the new shear wave velocity can be calculated

$$V_s = \sqrt{\frac{G}{\rho_B}}. \tag{2.14}$$

This concludes the fluid substitution and the updated model can now be used for additional seismic modelling.

2.2 Time-lapse imaging and interferometry

In this thesis two methods are described for time-lapse imaging; one that uses a time-convolution type integral and another that uses a time-correlation type integral. The former produces a difference wave field containing difference refections, the latter, which is an interferometric method, yields phase differences.

The time-convolution type integral is used to construct a difference wave field from two time-lapse wave fields by calculating a surface integral at a certain level in the sub-surface. The interesting feature of this difference wave field is that it contains information about time-lapse changes below the level at which the integral is calculated (Dillen, 2000). Any changes above this level will not contribute to the resulting difference reflections.

Similarly, the time-correlation type integral, representing an interferometric method, can also be computed at depth, yielding a difference phase map unaffected by the time-lapse changes above the surface of computation. Hence, both the time-convolution type and the time-correlation type methods offer a recursive scheme which can unravel the time-lapse changes from the wave fields, starting at the acquisition surface and working through the overburden towards the target of interest. The output yields images in terms of true time-lapse reflectivity or phases depending on which method is chosen.

In order to compute the surface integral at depth, the wave field at the desired depth has to be known. The way to obtain this is through back-propagation from the receivers down to the desired depth. When doing synthetic modelling another option is placing the receivers at the target depth in the model to record the required wave fields. The synthetic approach will be followed in this thesis.

2.2.1 Acoustic wave equations

A media defined by the parameters $\{\rho, \kappa\}$, ρ being the density and κ being the bulk modulus as discussed in Chapter 2.1, is considered. Being an acoustic medium, the shear modules is defined as zero. For this medium the acoustic wave equations are defined as

$$\partial_k p(\boldsymbol{x}; \boldsymbol{x}_S, t) + \rho(\boldsymbol{x})\partial_t v_k(\boldsymbol{x}; \boldsymbol{x}_S, t) = f_k(t)\delta(\boldsymbol{x} - \boldsymbol{x}_S), \tag{2.15}$$

$$\partial_k v_k(\boldsymbol{x}; \boldsymbol{x}_S, t) + \kappa(\boldsymbol{x})\partial_t p(\boldsymbol{x}; \boldsymbol{x}_S, t) = q(t)\delta(\boldsymbol{x} - \boldsymbol{x}_S) \tag{2.16}$$

where $v_k(\boldsymbol{x}; \boldsymbol{x}_S, t)$ is k-th component of the particle velocity at $\boldsymbol{x}$ due to a source at $\boldsymbol{x}_S$ and $p(\boldsymbol{x}; \boldsymbol{x}_S, t)$ is the pressure at $\boldsymbol{x}$ caused by a source at $\boldsymbol{x}_S$. $f_k(t)$ is a displacement source and $q(t)$ is a volumetric source. A description of the notation used is given in Chapter 1.2.

Now consider two sets of time-lapse acoustic wave fields, the *reference* and the *monitor* wave field, denoted by superscripts $^{(1)}$ and $^{(2)}$ respectively.

The Fourier transforms of Eqs. (2.15) and (2.16) for these *reference* and *monitor* wave fields are then given as

$$\partial_k \hat{p}^{(1)}(\boldsymbol{x}; \boldsymbol{x}_S^{(1)}, \omega) + \mathrm{i}\omega\rho^{(1)}(\boldsymbol{x})\hat{v}_k^{(1)}(\boldsymbol{x}; \boldsymbol{x}_S^{(1)}, \omega) = \hat{f}_k^{(1)}(\omega)\delta(\boldsymbol{x} - \boldsymbol{x}_S^{(1)}) \tag{2.17}$$

$$\partial_k \hat{v}_k^{(1)}(\boldsymbol{x}; \boldsymbol{x}_S^{(1)}, \omega) + \mathrm{i}\omega\kappa^{(1)}(\boldsymbol{x})\hat{p}^{(1)}(\boldsymbol{x}; \boldsymbol{x}_S^{(1)}, \omega) = \hat{q}^{(1)}(\omega)\delta(\boldsymbol{x} - \boldsymbol{x}_S^{(1)}), \tag{2.18}$$

and

$$\partial_k \hat{p}^{(2)}(\boldsymbol{x}; \boldsymbol{x}_S^{(2)}, \omega) + \mathrm{i}\omega\rho^{(2)}(\boldsymbol{x})\hat{v}_k^{(2)}(\boldsymbol{x}; \boldsymbol{x}_S^{(2)}, \omega) = \hat{f}_k^{(2)}(\omega)\delta(\boldsymbol{x} - \boldsymbol{x}_S^{(2)}) \tag{2.19}$$

$$\partial_k \hat{v}_k^{(2)}(\boldsymbol{x}; \boldsymbol{x}_S^{(2)}, \omega) + \mathrm{i}\omega\kappa^{(2)}(\boldsymbol{x})\hat{p}^{(2)}(\boldsymbol{x}; \boldsymbol{x}_S^{(2)}, \omega) = \hat{q}^{(2)}(\omega)\delta(\boldsymbol{x} - \boldsymbol{x}_S^{(2)}), \tag{2.20}$$

respectively. For readability and simplicity the arguments will later be dropped from most equations.

2.2.2 Acoustic reciprocity of the convolution type

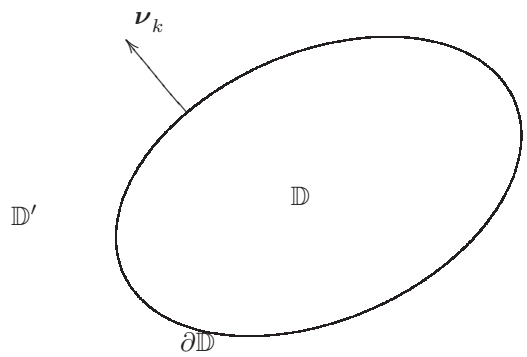

Fig. 2.1: Configuration for the application of the reciprocity theorem.

The interaction quantity between the two time-lapse states is given by the field reciprocity relationship as (Fokkema and van den Berg, 1993)

$$\partial_k(\hat{p}^{(1)}\hat{v}_k^{(2)}-\hat{p}^{(2)}\hat{v}_k^{(1)}) = \hat{v}_k^{(2)}\partial_k\hat{p}^{(1)}+\hat{p}^{(1)}\partial_k\hat{v}_k^{(2)}-\hat{v}_k^{(1)}\partial_k\hat{p}^{(2)}-\hat{p}^{(2)}\partial_k\hat{v}_k^{(1)} \quad (2.21)$$

By multiplying Eqs. (2.17)–(2.20) by $\hat{v}_k^{(2)}$, $\hat{p}^{(2)}$, $\hat{v}_k^{(1)}$ and $\hat{p}^{(1)}$ respectively the following expressions are obtained

$$\hat{v}_k^{(2)}\partial_k\hat{p}^{(1)} + \mathrm{i}\omega\rho^{(1)}\hat{v}_k^{(1)}\hat{v}_k^{(2)} = \hat{f}_k^{(1)}\hat{v}_k^{(2)} \quad (2.22)$$

$$\hat{p}^{(2)}\partial_k\hat{v}_k^{(1)} + \mathrm{i}\omega\kappa^{(1)}\hat{p}^{(1)}\hat{p}^{(2)} = \hat{q}^{(1)}\hat{p}^{(2)} \quad (2.23)$$

$$\hat{v}_k^{(1)}\partial_k\hat{p}^{(2)} + \mathrm{i}\omega\rho^{(2)}\hat{v}_k^{(2)}\hat{v}_k^{(1)} = \hat{f}_k^{(1)}\hat{v}_k^{(1)} \quad (2.24)$$

$$\hat{p}^{(1)}\partial_k\hat{v}_k^{(2)} + \mathrm{i}\omega\kappa^{(2)}\hat{p}^{(2)}\hat{p}^{(1)} = \hat{q}^{(2)}\hat{p}^{(1)} \quad (2.25)$$

By applying Eqs. (2.22)–(2.25) to Eq. (2.21) one arrives at the following relationship

$$\partial_k(\hat{p}^{(1)}\hat{v}_k^{(2)} - \hat{p}^{(2)}\hat{v}_k^{(1)}) = \mathrm{i}\omega\left\{(\rho^{(2)}-\rho^{(1)})\hat{v}_k^{(1)}\hat{v}_k^{(2)} - (\kappa^{(2)}-\kappa^{(1)})\hat{p}^{(1)}\hat{p}^{(2)}\right\} + \hat{f}^{(1)}\hat{v}_k^{(2)} + \hat{q}^{(2)}\hat{p}^{(1)} - \hat{f}^{(2)}\hat{v}_k^{(1)} - \hat{q}^{(1)}\hat{p}^{(2)} \quad (2.26)$$

which is the local form of Rayleigh's reciprocity theorem.

Integrating Eq. (2.26) over the domain $\mathbb{D}$ and applying Gauss' integral theorem to the resulting integral on the left hand side yields

$$\int\limits_{\partial\mathbb{D}} \left(\hat{p}^{(1)}\hat{v}_k^{(2)} - \hat{p}^{(2)}\hat{v}_k^{(1)}\right)\nu_k \mathrm{dA}$$
$$= \int\limits_{\mathbb{D}} \mathrm{i}\omega \left((\rho^{(2)} - \rho^{(1)})\hat{v}_k^{(1)}\hat{v}_k^{(2)} - (\kappa^{(2)} - \kappa^{(1)})\hat{p}^{(1)}\hat{p}^{(2)}\right) \mathrm{dV}$$
$$+ \int\limits_{\mathbb{D}} \left(\hat{f}_k^{(1)}\hat{v}_k^{(2)} + \hat{q}^{(2)}\hat{p}^{(1)} - \hat{f}_k^{(2)}\hat{v}_k^{(1)} - \hat{q}^{(1)}\hat{p}^{(2)}\right) \mathrm{dV} \quad (2.27)$$

where ν is the normal vector of $\partial\mathbb{D}$, the first volume integral on the right hand side represents the media contrast and the right-most volume integral is the source term. Eq. (2.27) is the global form of Rayleigh's reciprocity theorem for the domain $\mathbb{D}$. It represents the complex-frequency domain reciprocity theorem of the time-convolution type (the multiplications represent convolutions in the time-domain).

Now, using only explosive point sources, defined in Eq. (2.71), Eq. (2.27) simplifies to

$$\int_{\boldsymbol{x}\in\partial\mathbb{D}} \left(\hat{v}_k^{(1)}(\boldsymbol{x};\boldsymbol{x}_S^{(1)})\hat{p}^{(2)}(\boldsymbol{x};\boldsymbol{x}_S^{(2)}) - \hat{p}^{(1)}(\boldsymbol{x};\boldsymbol{x}_S^{(1)})\hat{v}_k^{(2)}(\boldsymbol{x};\boldsymbol{x}_S^{(2)})\right)\nu_k \mathrm{dA}$$
$$+ \mathrm{i}\omega \int_{\boldsymbol{x}\in\mathbb{D}} \left(\Delta\rho\hat{v}_k^{(1)}(\boldsymbol{x};\boldsymbol{x}_S^{(1)})\hat{v}_k^{(2)}(\boldsymbol{x};\boldsymbol{x}_S^{(2)}) - \Delta\kappa\hat{p}^{(1)}(\boldsymbol{x};\boldsymbol{x}_S^{(1)})\hat{p}^{(2)}(\boldsymbol{x};\boldsymbol{x}_S^{(2)})\right) \mathrm{dV}$$
$$= \hat{q}^{(1)}\hat{p}^{(2)}(\boldsymbol{x}_S^{(1)};\boldsymbol{x}_S^{(2)}) - \hat{q}^{(2)}\hat{p}^{(1)}(\boldsymbol{x}_S^{(2)};\boldsymbol{x}_S^{(1)}), \quad (2.28)$$

where Δ is the contrast between properties of the two cases, such that given γ as a property of either the wavefields or media

$$\Delta\gamma = \gamma^{(2)} - \gamma^{(1)}. \quad (2.29)$$

Eq. (2.28) shows that the sum of a boundary integral and a volume integral containing temporal contrast sources is equivalent to a difference field (see e.g. Dillen, 2000).

If one considers the case where both sources are within the domain $\mathbb{D}$ and there is no contrast in medium parameters between the reference and monitor model, i.e. $\kappa^{(1)} = \kappa(2)$ and $\rho^{(1)} = \rho^{(2)}$, the second integral on the left hand side of Eq. (2.28) will vanish. If in addition the medium is unbounded such that $\partial\mathbb{D} \to \infty$ the contribution from the boundary integral will also disappear (Fokkema and van den Berg, 1993) (see Fig. 2.2), leaving

$$0 = \hat{q}^{(1)}\hat{p}^{(2)}(\boldsymbol{x}_S^{(1)};\boldsymbol{x}_S^{(2)}) - \hat{q}^{(2)}\hat{p}^{(1)}(\boldsymbol{x}_S^{(2)};\boldsymbol{x}_S^{(1)}) \quad (2.30)$$

When the source signature is the same, i.e. $\hat{q}^{(1)} = \hat{q}^{(2)}$, it follows from Eq. (2.30) that for any state

$$\hat{p}(\boldsymbol{x}_S^{(1)};\boldsymbol{x}_S^{(2)}) = \hat{p}(\boldsymbol{x}_S^{(2)};\boldsymbol{x}_S^{(1)}) \quad (2.31)$$

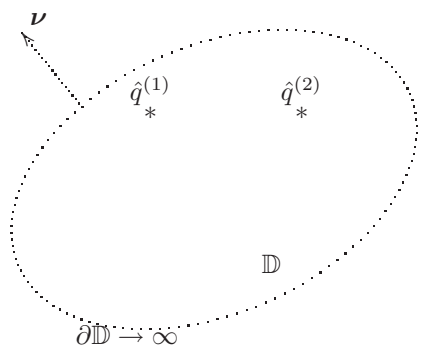

Fig. 2.2: Unbounded media with no time-lapse contrast.

which is to say that the fields recorded from each of the two shots are interchangeable. Using this source-receiver reciprocity and assuming equal sources simplifies the right-hand side of Eq. (2.28) to

$$\hat{q}^{(1)}\hat{p}^{(2)}(\boldsymbol{x}_S^{(1)};\boldsymbol{x}_S^{(2)}) - \hat{q}^{(2)}\hat{p}^{(1)}(\boldsymbol{x}_S^{(2)};\boldsymbol{x}_S^{(1)}) = \hat{q}\Delta\hat{p}(\boldsymbol{x}_S^{(1)};\boldsymbol{x}_S^{(2)}) \tag{2.32}$$

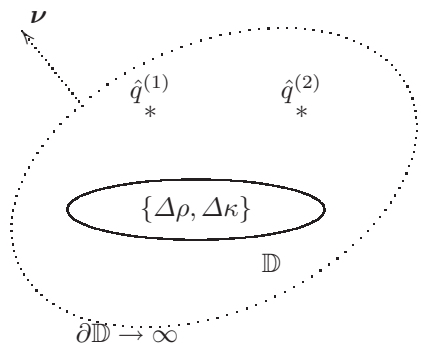

Fig. 2.3: Unbounded media with contrast volume.

Having examined the situation where there is no change in the medium parameters, the next step is to look at the situation where there are changes in medium parameters, as illustrated by Fig. 2.3. Applying Eq. (2.28), the contribution from the boundary integral becomes zero, but the medium contrast will have an effect through the volume integral, leading to, using Eq. (2.32)

$$\mathrm{i}\omega \int_{\boldsymbol{x}\in\mathbb{D}} \Big(\Delta\rho \hat{v}_k^{(1)}(\boldsymbol{x};\boldsymbol{x}_S^{(1)})\hat{v}_k^{(2)}(\boldsymbol{x};\boldsymbol{x}_S^{(2)}) - \Delta\kappa \hat{p}^{(1)}(\boldsymbol{x};\boldsymbol{x}_S^{(1)})\hat{p}^{(2)}(\boldsymbol{x};\boldsymbol{x}_S^{(2)}) \Big)\,\mathrm{dV} = \hat{q}\Delta\hat{p}(\boldsymbol{x}_S^{(1)};\boldsymbol{x}_S^{(2)}) \quad (2.33)$$

which shows that the difference wave field is equal to an integral over the temporal contrast sources.

2.2.3 Interaction integral

Taking the boundary integral of Eq. (2.28) the following interaction integral is defined (Dillen, 2000; Dillen et al., 2002)

$$\hat{I}_{conv}(x_3^c;\boldsymbol{x}_S^{(1)},\boldsymbol{x}_S^{(2)}) \stackrel{\text{def}}{=} \int_{\boldsymbol{x}_T\in\mathbb{R}^2} \Big(\hat{v}_3^{(1)}(\boldsymbol{x}_T,x_3^c;\boldsymbol{x}_S^{(1)})\hat{p}^{(2)}(\boldsymbol{x}_T,x_3^c;\boldsymbol{x}_S^{(2)}) - \hat{v}_3^{(2)}(\boldsymbol{x}_T,x_3^c;\boldsymbol{x}_S^{(2)})\hat{p}^{(1)}(\boldsymbol{x}_T,x_3^c;\boldsymbol{x}_S^{(1)}) \Big)\mathrm{d}\boldsymbol{x}_T \quad (2.34)$$

where x_3^c is the depth where the integral is evaluated, and $\boldsymbol{x}_T = (x_1, x_2)$ is the transverse coordinate over which the integration is performed. Fig. 2.4a shows a configuration where $x_3 = x_3^c$ represents the lower bounding surface of the domain of application $\mathbb{D}$. In defining the interaction integral it is taken into account, as indicated in the figures below, that the contributions where the boundary approaches infinity vanishes (Fokkema and van den Berg, 1993), so that only the contribution from the plane surface at $x_3 = x_3^c$ remains.

Fig. 2.4a shows the situation where the interaction integral is derived as a difference gather. Application of Eq. (2.28) to the configuration of Fig. 2.4a, taking into account that the time-lapse contrasts are outside $\mathbb{D}$, and using Eqs. (2.32) and (2.34), yields

$$\hat{I}_{conv}(x_3^c;\boldsymbol{x}_S^{(1)},\boldsymbol{x}_S^{(2)}) = \hat{q}\Delta\hat{p}(\boldsymbol{x}_S^{(1)};\boldsymbol{x}_S^{(2)}) \quad (2.35)$$

From this last equation it is clear that for any level between the sources and the top of the contrast volume, the interaction integral is invariant with respect to x_3.

If the domain of integration is as shown in Fig. 2.4b there are no sources within the domain. However, the time-lapse contrast will contribute such that Eq. (2.28) becomes

$$\hat{I}_{conv}(x_3^c;\boldsymbol{x}_S^{(1)},\boldsymbol{x}_S^{(2)}) = \mathrm{i}\omega \int_{\boldsymbol{x}\in\mathbb{D}_{tlc}} \Big(\Delta\kappa \hat{p}^{(1)}(\boldsymbol{x};\boldsymbol{x}_S^{(1)})\hat{p}^{(2)}(\boldsymbol{x};\boldsymbol{x}_S^{(2)}) - \Delta\rho \hat{v}_k^{(1)}(\boldsymbol{x};\boldsymbol{x}_S^{(1)})\hat{v}_k^{(2)}(\boldsymbol{x};\boldsymbol{x}_S^{(2)}) \Big)\mathrm{dV} \quad (2.36)$$

In this last equation $\mathbb{D}_{tlc}$ is the domain of time-lapse changes. Hence, the interaction integral is a measure of the total time-lapse changes below x_3^c.

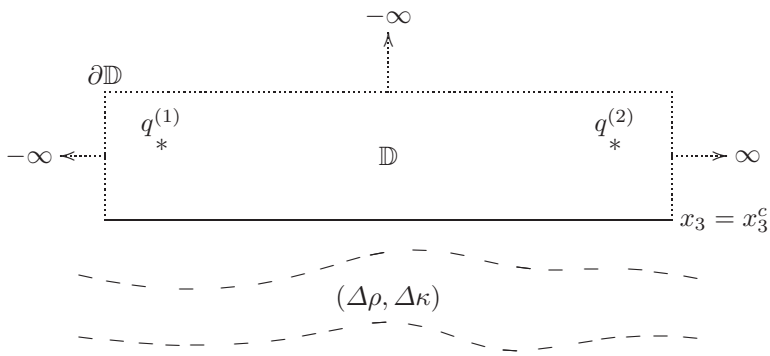

(a) Including sources, excluding contrast.

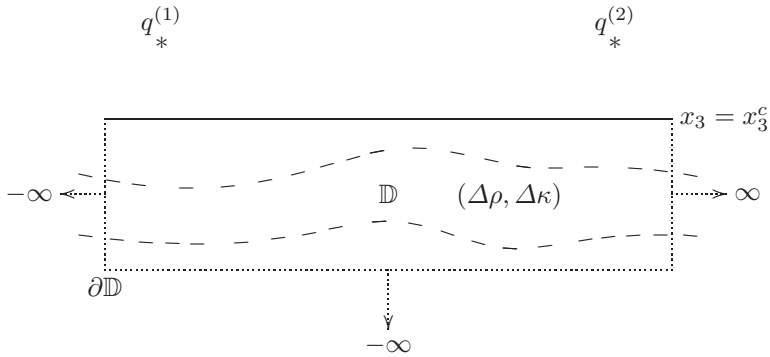

(b) Excluding sources, including contrast.

Fig. 2.4: Boundary integral evaluated above contrast.

When the interaction integral is evaluated at a depth inside the medium of time-lapse changes, as depicted in Figs. 2.5a and 2.5b, we can again derive two representations for $\hat{I}_{conv}$. For the upper figure we obtain

$$\begin{aligned}\hat{I}_{conv}(x_3^c; \boldsymbol{x}_S^{(1)}, \boldsymbol{x}_S^{(2)}) &= \hat{q}\Delta\hat{p}(\boldsymbol{x}_S^{(1)}; \boldsymbol{x}_S^{(2)}) \\ &- \mathrm{i}\omega \iint\limits_{\substack{\boldsymbol{x}_T \in \mathbb{R}^2 \\ x_3^{min} < x_3 < x_3^c}} \Big(\Delta\rho \hat{v}_k^{(1)}(x_3, \boldsymbol{x}_T; \boldsymbol{x}_S^{(1)}) \hat{v}_k^{(2)}(x_3, \boldsymbol{x}_T; \boldsymbol{x}_S^{(2)}) \\ &\qquad - \Delta\kappa \hat{p}^{(1)}(x_3, \boldsymbol{x}_T; \boldsymbol{x}_S^{(1)}) \hat{p}^{(2)}(x_3, \boldsymbol{x}_T; \boldsymbol{x}_S^{(2)}) \Big) \mathrm{d}\boldsymbol{x}_T \mathrm{d}x_3, \quad (2.37)\end{aligned}$$

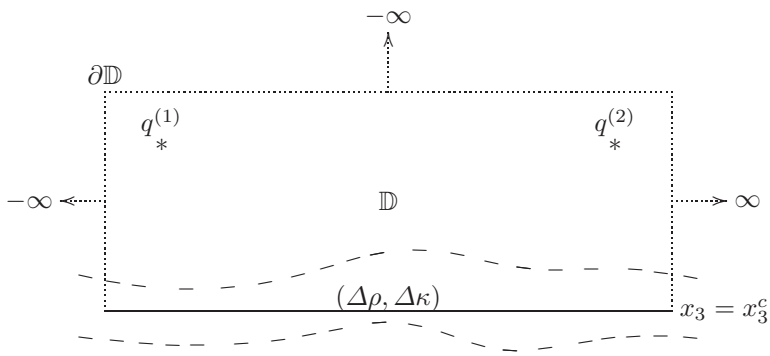

(a) Upper domain.

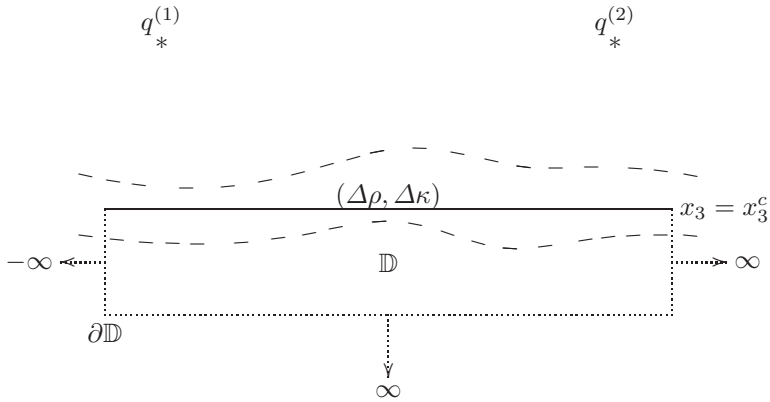

(b) Lower domain.

Fig. 2.5: Boundary integral evaluated inside contrast.

in which $\boldsymbol{x}_T$ is the transverse coordinate, x_3 is the longitudinal coordinate and x_3^{min} is the lower bound of the longitudinal coordinate in $\mathbb{D}_{tlc}$. A comparison shows that Eq. (2.37) contains the same difference wave field as Eq. (2.35), in addition to a sort of compensation term in the form of a volume integral with time-lapse contrast contributions between $x_3^{min} < x_3 < x_3^c$. Theoretical considerations (Dillen et al., 2002) and numerical modelling (this thesis) show that the latter volume integral removes the time-lapse effects caused by time-lapse contrasts inside $x_3^{min} < x_3 < x_3^c$ from the difference wave field $\Delta\hat{p}$. The volume integral is what will compensate for and eliminate the difference reflection originating at any level above x_3^c.

If the configuration is as shown in Fig. 2.5b the interaction integral $\hat{I}_{conv}$ contains information from the time-lapse contrasts inside $x_3^c < x_3 < x_3^{max}$,

with x_3^{max} being the upper bound of x_3 in $\mathbb{D}^{tlc}$;

$$\begin{aligned}\hat{I}_{conv}(x_3^c;\boldsymbol{x}_S^{(1)},\boldsymbol{x}_S^{(2)}) \\ &= i\omega \iint\limits_{\substack{\boldsymbol{x}_T\in\mathbb{R}^2\\ x_3^c<x_3<x_3^{max}}} \Big(\Delta\kappa\hat{p}^{(1)}(x_3,\boldsymbol{x}_T;\boldsymbol{x}_S^{(1)})\hat{p}^{(2)}(x_3,\boldsymbol{x}_T;\boldsymbol{x}_S^{(2)}) \\ &\qquad - \Delta\rho\hat{v}_k^{(1)}(x_3,\boldsymbol{x}_T;\boldsymbol{x}_S^{(1)})\hat{v}_k^{(2)}(x_3,\boldsymbol{x}_T;\boldsymbol{x}_S^{(2)})\Big)\mathrm{d}\boldsymbol{x}_T\mathrm{dx}_3 \qquad (2.38)\end{aligned}$$

Comparison with Eq. (2.36) shows that in Eq. (2.38) $\hat{I}_{conv}$ is influenced by an smaller amount of the contrast volume as x_3^c passes through the changes.

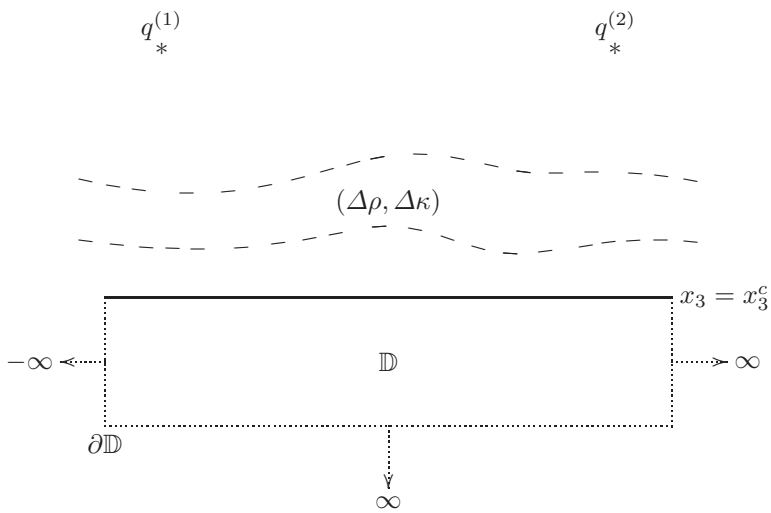

Fig. 2.6: Boundary integral evaluated below contrast.

In Fig. 2.6 a situation where the boundary integral is evaluated at a level below the contrast is shown. For this situation the interaction integral is zero, since neither the sources of the difference wave field nor the contrast volume give any contribution;

$$I_{conv}(x_3^c;\boldsymbol{x}_S^{(1)},\boldsymbol{x}_S^{(2)}) = 0 \qquad (2.39)$$

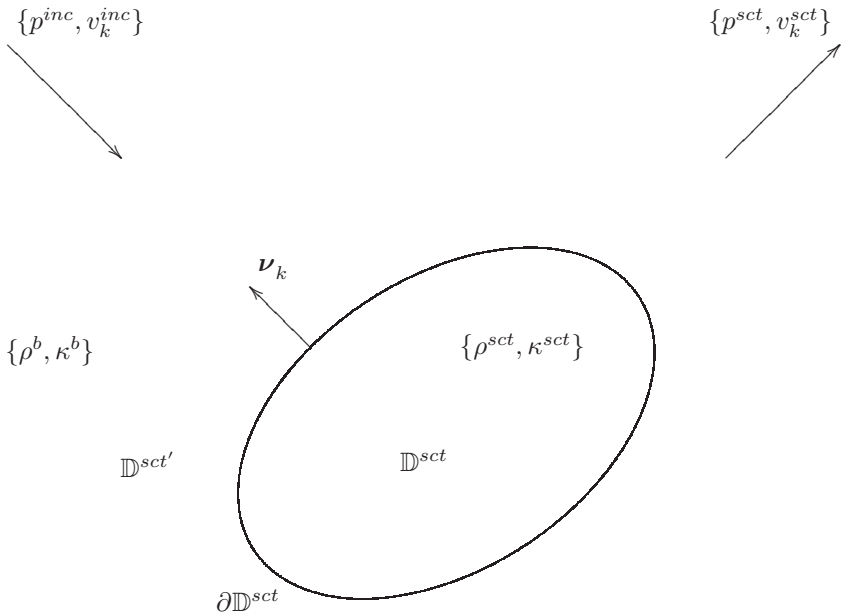

Fig. 2.7: Scattering domain.

2.2.4 Scattered wave fields

Scattered wave fields are caused by a contrast between an embedded medium and a background medium of infinite extent in which it is embedded, as illustrated in Fig. 2.7. In terms of the medium perturbation $\{\delta\rho, \delta\kappa\}$ we write

$$\{\rho, \kappa\} = \{\rho^b, \kappa^b\} \quad \text{in} \quad \mathbb{D}^{sct'}, \tag{2.40}$$

$$\{\rho, \kappa\} = \{\rho^{sct}, \kappa^{sct}\} = \{\rho^b, \kappa^b\} + \{\delta\rho, \delta\kappa\} \quad \text{in} \quad \mathbb{D}^{sct}, \tag{2.41}$$

where the contrasting medium in the domain $\mathbb{D}^{sct}$ is defined by the parameters $\{\rho^{sct}, \kappa^{sct}\}$. Its complement with respect to $\mathbb{R}^3$ and its boundary $\partial\mathbb{D}^{sct}$ is denoted by $\mathbb{D}^{sct'}$. In $\mathbb{R}^3$ the background medium parameters are denoted by $\{\rho^b, \kappa^b\}$

The total acoustic wave field in the configuration, $\{\hat{p}, \hat{v}_k\}$, is decomposed into an incident wave field, $\{\hat{p}^{inc}, \hat{v}_k^{inc}\}$, and a scattered wave field, $\{\hat{p}^{sct}, \hat{v}_k^{sct}\}$;

$$\hat{p} = \hat{p}^{sct} + \hat{p}^{inc}, \tag{2.42}$$

$$\hat{v}_k = \hat{v}_k^{sct} + \hat{v}_k^{inc}. \tag{2.43}$$

The incident wave field is the wave field which would be present even if $\mathbb{D}^{sct}$ shows no contrast to the background. The source of the total wave field is

outside the scattering domain, and since it remains in the absence of the scattering domain it also serves as the source for the incident wave field.

The goal now is to find an expression for the scattered wave field which shows that it originates from the contrast in acoustic parameters between the scattering domain and the background media. First it is established that since the total wave field has no sources within the scattering domain;

$$\partial_k \hat{p} + \mathrm{i}\omega\rho^{sct}\hat{v}_k = 0, \quad \text{in} \quad \mathbb{D}^{sct}, \tag{2.44}$$

$$\partial_k \hat{v}_k + \mathrm{i}\omega\kappa^{sct}\hat{p} = 0, \quad \text{in} \quad \mathbb{D}^{sct}. \tag{2.45}$$

Next, it is observed that the incident wave field also has no sources in $\mathbb{D}^{sct}$, and is defined by the material parameters of the background material.

$$\partial_k \hat{p}^{inc} + \mathrm{i}\omega\rho^{b}\hat{v}_k^{inc} = 0, \quad \text{in} \quad \mathbb{D}^{sct}, \tag{2.46}$$

$$\partial_k \hat{v}_k^{inc} + \mathrm{i}\omega\kappa^{b}\hat{p}^{inc} = 0, \quad \text{in} \quad \mathbb{D}^{sct}. \tag{2.47}$$

Eqs. (2.44) and (2.45) can be rewritten as

$$\partial_k \hat{p} + \mathrm{i}\omega\rho^{b}\hat{v}_k = -\mathrm{i}\omega\delta\rho\hat{v}_k, \quad \text{in} \quad \mathbb{D}^{sct}, \tag{2.48}$$

$$\partial_k \hat{v}_k + \mathrm{i}\omega\kappa^{b}\hat{p} = -\mathrm{i}\omega\delta\kappa\hat{p}, \quad \text{in} \quad \mathbb{D}^{sct}. \tag{2.49}$$

By subtracting Eqs. (2.46) and (2.47) from Eqs. (2.48) and (2.49), respectively, while applying Eqs. (2.43) and (2.42), the following relationship emerges

$$\partial_k \hat{p}^{sct} + \mathrm{i}\omega\rho^{b}\hat{v}_k^{sct} = -\mathrm{i}\omega\delta\rho\hat{v}_k, \quad \text{in} \quad \mathbb{D}^{sct}, \tag{2.50}$$

$$\partial_k \hat{v}_k^{sct} + \mathrm{i}\omega\kappa^{b}\hat{p}^{sct} = -\mathrm{i}\omega\delta\kappa\hat{p}, \quad \text{in} \quad \mathbb{D}^{sct}. \tag{2.51}$$

There are no sources for the scattered wave field outside the scattering domain, therefore

$$\partial_k \hat{p}^{sct} + \mathrm{i}\omega\rho^{b}\hat{v}_k^{sc} = 0, \quad \text{in} \quad \mathbb{D}^{sct'}, \tag{2.52}$$

$$\partial_k \hat{v}_k^{sct} + \mathrm{i}\omega\kappa^{b}\hat{p}^{sct} = 0, \quad \text{in} \quad \mathbb{D}^{sct'}. \tag{2.53}$$

By combining Eqs. (2.50)–(2.53) the following result is obtained

$$\partial_k \hat{p}^{sct} + \mathrm{i}\omega\rho^{b}\hat{v}_k^{sct} = \hat{f}_k^{sct}, \quad \text{in} \quad \mathbb{R}^3, \tag{2.54}$$

$$\partial_k \hat{v}_k^{sct} + \mathrm{i}\omega\kappa^{b}\hat{p}^{sct} = \hat{q}^{sct}, \quad \text{in} \quad \mathbb{R}^3, \tag{2.55}$$

where

$$\hat{f}_k^{sct} = \{i\omega\delta\rho\hat{v}_k, 0\}, \quad \text{in} \quad \{\mathbb{D}^{sct}, \mathbb{D}^{sct'}\}, \tag{2.56}$$

$$\hat{q}^{sct} = \{i\omega\delta\kappa\hat{p}, 0\}, \quad \text{in} \quad \{\mathbb{D}^{sct}, \mathbb{D}^{sct'}\}. \tag{2.57}$$

2.2.5 Interferometry

Interferometry does not use the total wave field, as the interaction integral of the convolution type does, but instead depends on the scattered wave fields defined earlier.

In order to define the interaction integral of the time correlation type it is once again necessary to consider two states, denoted by superscripts $^{(1)}$ and $^{(2)}$. These are defined as described in Chapter 2.2.1. The important distinction is that now they are scattered wave fields, which according to Eqs. (2.54) and (2.55) are defined by

$$\partial_k \hat{p}^{sct,(1)} + \mathrm{i}\omega\rho^{b,(1)}\hat{v}_k^{sct,(1)} = \hat{f}_k^{sct,(1)}, \tag{2.58}$$

$$\partial_k \hat{v}_k^{sct,(1)} + \mathrm{i}\omega\kappa^{b,(1)}\hat{p}^{sct,(1)} = \hat{q}^{sct,(1)}, \tag{2.59}$$

and

$$\partial_k \hat{p}^{sct,(2)} + \mathrm{i}\omega\rho^{b,(2)}\hat{v}_k^{sct,(2)} = \hat{f}_k^{sct,(2)}, \tag{2.60}$$

$$\partial_k \hat{v}_k^{sct,(2)} + \mathrm{i}\omega\kappa^{b,(2)}\hat{p}^{sct,(2)} = \hat{q}^{sct,(2)}, \tag{2.61}$$

respectively. Now state $^{(2)}$ is characterised by the anti-causal wave field,

$$\{\hat{p}^{\ddagger sct,(2)}, \hat{v}_k^{\ddagger sct,(2)}\}(\boldsymbol{x},\omega) = \{\hat{p}^{sct,(2)}, \hat{v}_k^{sct,(2)}\}(\boldsymbol{x},-\omega), \tag{2.62}$$

with source distribution

$$\{\hat{q}^{\ddagger sct,(2)}, \hat{f}_k^{\ddagger sct,(2)}\}(\boldsymbol{x},\omega) = \{\hat{q}^{sct,(2)}, \hat{f}_k^{sct,(2)}\}(\boldsymbol{x},-\omega), \tag{2.63}$$

with complex conjugate denoted by ‡. The acoustic wave field equations for state $^{(2)}$ are

$$\partial_k \hat{p}^{sct,(2)\ddagger} - \mathrm{i}\omega\rho^{b,(2)}\hat{v}_k^{sct,(2)\ddagger} = \hat{f}_k^{sct,(2)\ddagger}, \tag{2.64}$$

$$\partial_k \hat{v}_k^{sct,(2)\ddagger} - \mathrm{i}\omega\kappa^{b,(2)}\hat{p}^{sct,(2)\ddagger} = \hat{q}^{sct,(2)\ddagger}, \tag{2.65}$$

The superscript ^{sct} used to denote scattered wave fields will be left out from later equations for the sake of readability, such that all wave fields are to be considered as scattered unless explicitly defined otherwise.

The interaction quantity between the two states is now given as

$$\begin{aligned}\partial_k(\hat{p}^{(1)}\hat{v}_k^{\ddagger(2)} + \hat{v}_k^{(1)}\hat{p}^{\ddagger(2)}) \\ = \hat{v}_k^{\ddagger(2)}\partial_k\hat{p}^{(1)} + \hat{p}^{(1)}\partial_k\hat{v}_k^{\ddagger(2)} + \hat{v}_k^{(1)}\partial_k\hat{p}^{\ddagger(2)} + \hat{p}^{\ddagger(2)}\partial_k\hat{v}_k^{(1)}.\end{aligned} \tag{2.66}$$

By multiplying Eqs. (2.58), (2.59), (2.64) and (2.65) by $\hat{v}_k^{\ddagger sct,(2)}$, $\hat{p}^{\ddagger sct,(2)}$, $\hat{v}_k^{sct,(1)}$ and $\hat{p}^{sct,(1)}$ respectively, and using Eq. (2.66) one arrives at

$$\partial_k(\hat{p}^{(1)}\hat{v}_k^{\ddagger(2)} + \hat{v}_k^{(1)}\hat{p}^{\ddagger(2)}) = \mathrm{i}\omega\left(\Delta\rho^b\hat{v}_k^{(1)}\hat{v}_k^{\ddagger(2)} + \Delta\kappa^b\hat{p}^{(1)}\hat{p}^{\ddagger(2)}\right) + \hat{f}_k^{(1)}\hat{v}_k^{\ddagger(2)} + \hat{f}_k^{\ddagger(2)}\hat{v}_k^{(1)} + \hat{q}^{\ddagger(2)}\hat{p}^{(1)} + \hat{q}^{(1)}\hat{p}^{\ddagger(2)}. \quad (2.67)$$

Integrating Eq. (2.67) over the domain $\mathbb{D}$ with boundary $\partial\mathbb{D}$ and with $\mathbb{D}^{sct} \subset \mathbb{D}$ leads to

$$\int_{\boldsymbol{x}\in\partial\mathbb{D}} \left(\hat{p}^{(1)}\hat{v}_k^{\ddagger(2)} + \hat{v}_k^{(1)}\hat{p}^{\ddagger(2)}\right)\nu_k \mathrm{dA} = \mathrm{i}\omega\int_{\boldsymbol{x}\in\mathbb{R}^3}\left(\Delta\rho^b\hat{v}_k^{(1)}\hat{v}_k^{\ddagger(2)} + \Delta\kappa^b\hat{p}^{(1)}\hat{p}^{\ddagger(2)}\right)\mathrm{dV} + \int_{\boldsymbol{x}\in\mathbb{D}^{sct}}\left(\hat{f}_k^{(1)}\hat{v}_k^{\ddagger(2)} + \hat{f}_k^{\ddagger(2)}\hat{v}_k^{(1)} + \hat{q}^{\ddagger(2)}\hat{p}^{(1)} + \hat{q}^{(1)}\hat{p}^{\ddagger(2)}\right)\mathrm{dV} \quad (2.68)$$

where we take into account that the contrast sources have support in $\mathbb{D}^{sct}$ only. Assuming the configuration in Fig. 2.2.5 we define

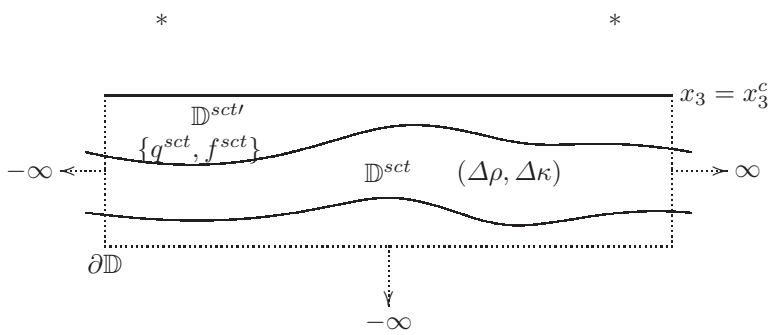

Fig. 2.8: Correlation integral above scatterer.

$$\hat{I}_{corr}(x_3^c; \boldsymbol{x}_S^{(1)}, \boldsymbol{x}_S^{(2)}) = \int_{x\in\mathbb{R}^2}\Big(\left[\hat{v}_k^{sct,(1)}(\boldsymbol{x}_T, x_3^c; \boldsymbol{x}_S^{(1)})\right]^{\ddagger}\hat{p}^{sct,(2)}(\boldsymbol{x}_T, x_3^c; \boldsymbol{x}_S^{(2)}) + \left[\hat{p}^{sct,(1)}(\boldsymbol{x}_T, x_3^c; \boldsymbol{x}_S^{(1)})\right]^{\ddagger}\hat{v}_k^{sct,(2)}(\boldsymbol{x}_T, x_3^c; \boldsymbol{x}_S^{(2)})\Big)\mathrm{d}\boldsymbol{x}_T. \quad (2.69)$$

Assuming that there is no temporal change in the background media, $\Delta\rho^b = 0$ and $\Delta\kappa^b = 0$, the first integral on the right-hand-side of Eq. (2.68) vanishes. Substituting Eqs. (2.56) and (2.57) we obtain

$$\hat{I}_{corr} \approx \int_{\boldsymbol{x}\in\mathbb{D}^{sct}} i\omega\Big(\delta\rho^{(1)}\hat{v}_k^{(1)}\hat{v}_k^{\ddagger(2)} - \delta\rho^{(2)}\hat{v}_k^{\ddagger(2)}\hat{v}_k^{(1)} + \delta\kappa^{(2)}\hat{p}^{\ddagger(2)}\hat{p}^{(1)} - \delta\kappa^{(1)}\hat{p}^{(1)}\hat{p}^{\ddagger(2)}\Big)\mathrm{dV} \quad (2.70)$$

It is an approximation because the anti-causal wave fields has small contributions from the lower boundary. When there is no time-lapse contrast we have $\delta\rho^{(1)} = \delta\rho^{(2)}$ and $\delta\kappa^{(1)} = \delta\kappa^{(2)}$, and hence, $\hat{I}_{corr}$ is approximately zero. Therefore, $\hat{I}_{corr}$ is a measure for the time-lapse contrast in $\mathbb{D}^{sct}$.

2.3 Finite-difference modelling

A common way of solving differential equations numerically is by using the finite-difference method. This involves transforming a continuous differential equation into a discrete system which can be solved stepwise numerically. In our example the equation is the two-dimensional wave equation.

Several schemes have been developed for solving both the elastic and the acoustic two-dimensional wave equation by the finite-difference method, and the specifics of these are beyond the scope of this work.

The scheme used for the finite-difference modelling here is one developed by Holberg (1987). It is an explicit solution of the scalar wave equation given below

$$\left(\frac{1}{\rho c^2}\right)\frac{\partial^2 P}{\partial t^2} = \sum_{j=1}^{3}\frac{\partial}{\partial x_j}\left(\rho^{-1}\left(\frac{\partial P}{\partial x_j}\right)\right) + s, \quad (2.71)$$

where P represents pressure, ρ is the density, c is seismic velocity and s is some source term. The explicit solution from Holberg (1987) is then given as

$$\begin{aligned} P_{n+1} &= 2P_n - P_{n-1} + \kappa\left[d_x\left(\rho^{-1}d_y\left(P_n\right)\right) + d_z\left(\rho^{-1}d_z\left(P_n\right)\right)\right], \\ \kappa &= \rho c\left(\Delta t\right)^2, \end{aligned} \quad (2.72)$$

where n is the step number, Δt is the temporal sampling interval, $x = x_1$, $y = x_2$, $z = x_3$ and P_n represents pressure at time $t = n\Delta t$. The stability condition of Eq. (2.72) is given by the following Eq. (see Holberg, 1987, p. 653)

$$c\Delta t \leq \frac{\Delta x}{\pi}\sqrt{3}(1+E), \quad (2.73)$$

where Δx is the spatial sampling interval and E is the maximum error in the frequency response of the spatial differentiators. In application of the scheme the maximum allowed error in group velocity can be used for E, since phase errors are generally much smaller than error in group velocity (Holberg, 1987).

Another criteria for the stability of the finite-difference scheme is the number of grid points per shortest wave-length. For some schemes this require-

ment can be as high as 10 grid points per shortest wavelength (e.g Kelly et al., 1976), but the solution presented by Holberg (1987) requires only a minimum of 2.0-2.5 grid points per shortest wavelength to produce acceptable results.

There may still be some unwanted artifacts in the modeled results (Wild and Singh, 1998), but since this work does not include any comparison to real data this effect is not considered to be of significance.

Chapter 3
Seismic modelling

3.1 Geological model

The 2D geological model is the same as used by Kvam (2005, chapter 3 and 6). It is based on stacked data from a representative in-line from the Gullfaks field. The model consist of 11 layers where P-wave velocities have been determined from velocity analysis on real seismic data, as well as well logs (Kvam and Landrø, 2005, p. 42-43). Densities are also from well logs. The S-wave velocity field is derived from a linear $V_p - V_s$ ratio (Castagna et al., 1985).

A part of this model will later be used for finite-difference modelling of time-lapse changes by performing fluid substitution in the reservoir zone.

Table 3.1: Initial model parameters.

Layer no.	V_p (m/s)	V_s (m/s)	Density (kg/m^3)
1 (water)	1476	0	1000
2	1758	800	1800
3	2132	800	1900
4	2216	900	2000
5	2088	850	2100
6	2271	910	2118
7	2580	1180	2300
8 (reservoir)	2630	1340	2350
9	2710	1280	2200
10	2900	1400	2400
11	3100	1500	2500

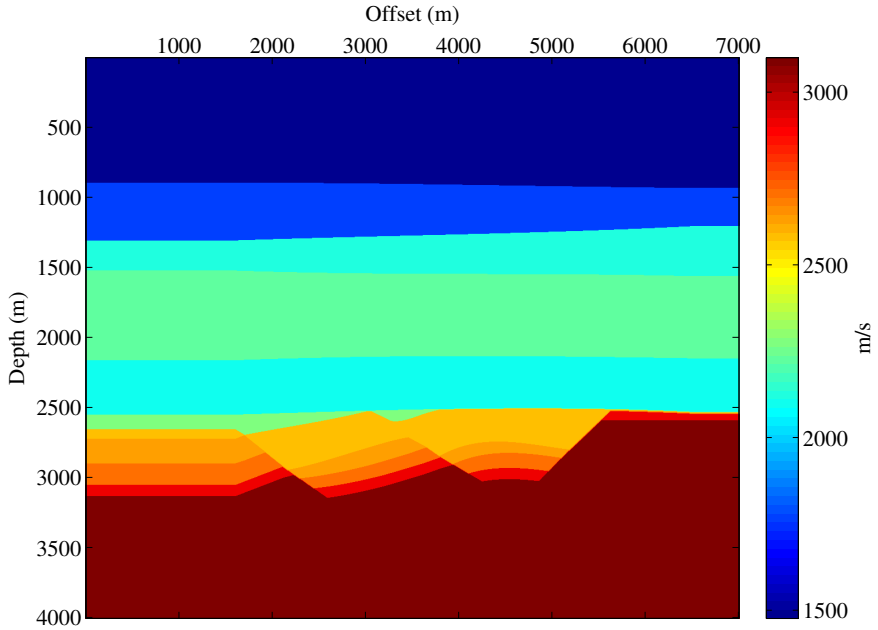

Fig. 3.1: P-wave velocity field for the complete model.

The dimensions of the full model are 7000 m in the horizontal direction and 4000 m in the vertical direction. The reservoir zone is at approximately 2700 m depth.

3.1.1 Partial model

To limit the computation time for modelling runs, a subset of the full model was created. This subset covers a graben-like structure containing part of the reservoir zone and parts of the basement and overburden and is 2000x2000 m. Fig. 3.2 shows the P-wave velocity field of the smaller model.

The test model is at a depth of 1600 m and an offset of 3600 m, as shown in figure 3.2.

3.2 Reservoir model

The parameters for the reservoir zone listed in Table 3.2 are from Stovas et al. (2006), while the pore water and oil properties are the same as used by Stovas and Landrø (2004).

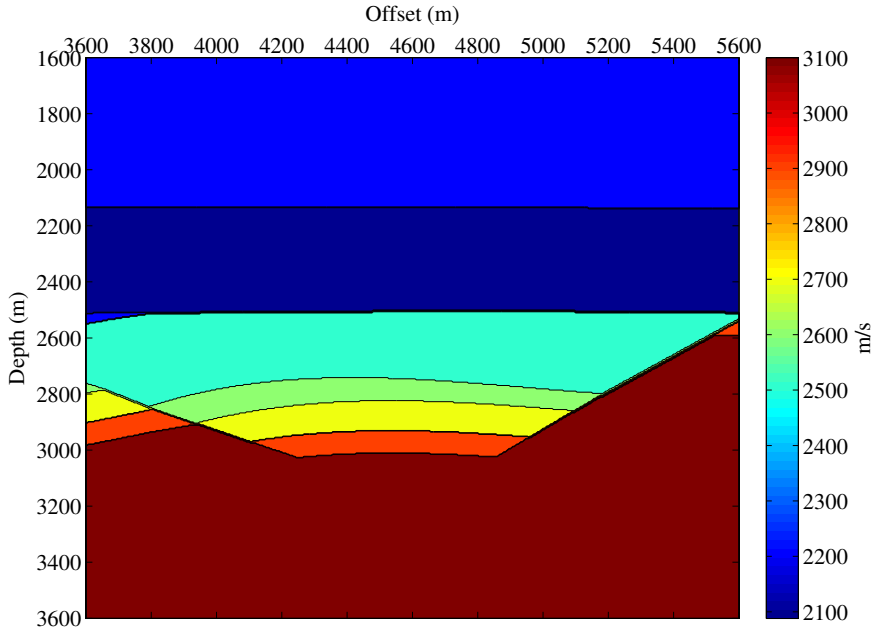

Fig. 3.2: Zoomed P-wave velocity field for reservoir part of geological model.

Table 3.2: Reservoir parameters.

S_0	K_{fr} (GPa)	K_{ma} (GPa)	μ (GPa)	ρ_{ma} (g/c^{3}m)	ϕ
0.29	4.70	29.0	3.91	2.62	0.29

3.3 Model calibration

Since the reservoir and fluid properties from Stovas et al. (2006) and Stovas and Landrø (2004) do not match the geological model from Kvam and Landrø (2005) the model has to be calibrated prior to fluid substitution. Initially attempts were made to adjust the two sets of parameters to match each other, but this proved to give unrealistic results. The chosen approach for calibration has been to replace the entire reservoir in the initial model from Kvam and Landrø (2005) with one where velocities and density are computed using rock and fluid properties from Stovas and Landrø (2004) and Stovas et al. (2006).

The density in the calibration is calculated using Eq. (2.4), where ρ_{fl} is found by applying Eq. (2.8) and ρ_{ma} is given in Table 3.2. To get the bulk density of the fluid Eqs. (2.9), (2.10) and (2.11) are used.

To determine the bulk modulus of the saturated reservoir Gassmann's equation (Gassmann, 1951) is used in the following form,

$$K = K_{fr} + \frac{4}{3}G + \frac{(K_{fr} - K_{ma})^2}{K_{ma}\left(1 - \phi + \phi\frac{K_{ma}}{K_f} - \frac{K_{fr}}{K_{ma}}\right)} \tag{3.1}$$

After obtaining K from Eq. (3.1) and G from Table 3.2 the initial seismic velocities are calculated from Eqs. (2.13) and (2.14). The pore fluids are assumed not to influence the shear modulus of the reservoir rock framework.

When the new initial properties are calculated they replace zone 8 in Table 3.1. The properties of the calibrated model are shown in Table 3.3.

Table 3.3: Calibrated model parameters.

Layer no.	V_p (m/s)	V_s (m/s)	Density (kg/m^3)
1 (water)	1476	0	1000
2	1758	800	1800
3	2132	800	1900
4	2216	900	2000
5	2088	850	2100
6	2271	910	2118
7	2580	1180	2300
8 (reservoir)	2482	1364	2100
9	2710	1280	2200
10	2900	1400	2400
11	3100	1500	2500

3.4 Modelling software

The software used for modelling is SDI (Amundsen et al., 1997). It is developed and supplied by SINTEF Petroleum Research, and is based on the finite-difference scheme developed by Holberg (1987). It is capable of doing acoustic or elastic modelling, but for simplicity and speed only acoustic modelling was used.

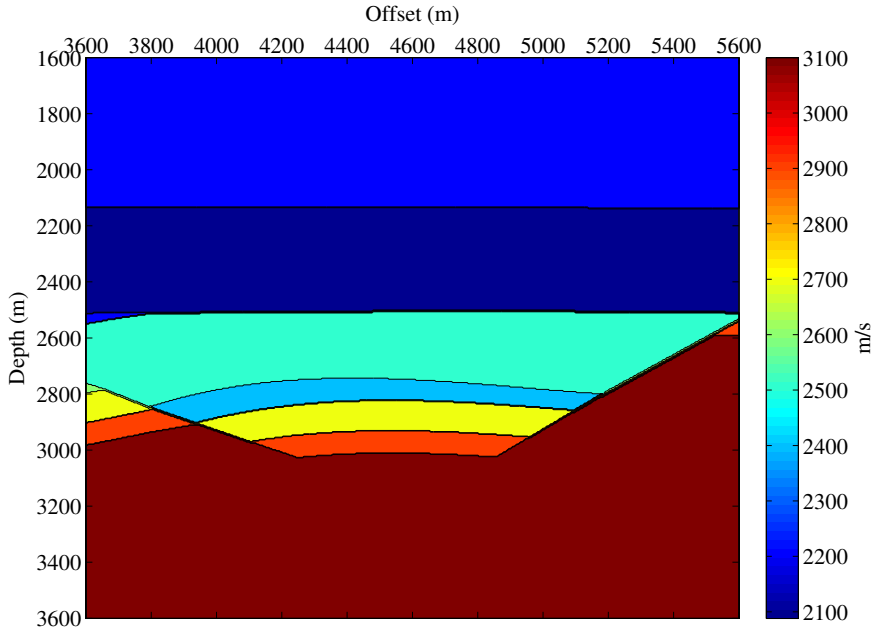

Fig. 3.3: P-wave velocity field for reservoir part of geological model after calibration.

3.5 Survey parameters

For each of the three scenarios, 11 different surveys have been modelled with receivers at different levels of the model. All parameters have been kept constant between the surveys except for the depth of the receiver level. More on this can be found in Chapter 3.5.2.

All distances in the survey geometry have to be multiples of the grid sizes (Δx and Δz). This is a restriction imposed by the modelling software.

3.5.1 Source

The source wavelet used is a second derivative Gaussian wavelet (Eq. (3.2)), with a maximum frequency of 50 Hz, and a dominant frequency of 22 Hz.

$$g(t) = \left(\left(2\sigma\left(t - t_0\right)\right)^2 - 2\sigma \right) e^{-\sigma\left(t-t_0\right)^2}, \tag{3.2}$$

where σ is the standard deviation of the Gaussian distribution, and t_0 is the time-shift of the Gaussian wavelet.

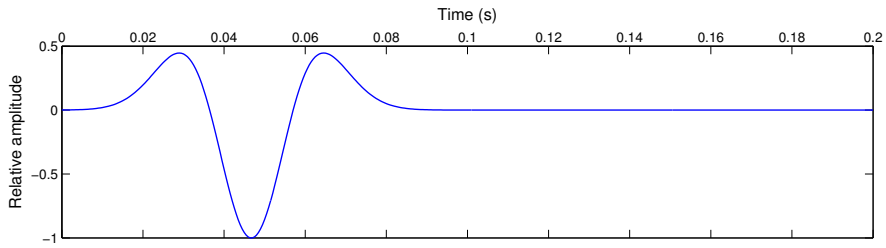

(a) Waveform.

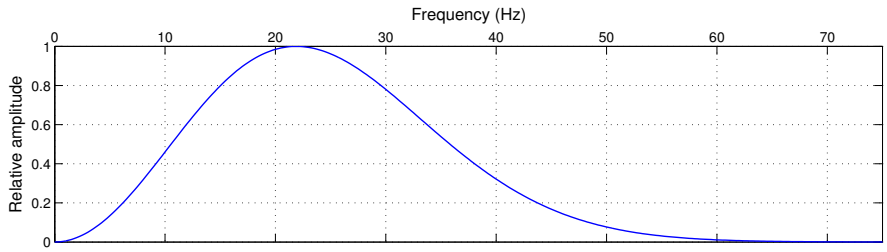

(b) Amplitude spectrum.

Fig. 3.4: Source wavelet.

3.5.2 Acquisition geometry

The same basic geometry are used for all the seismic experiments. The only parameter that might vary is the depth of the receiver level.

For every receiver level there are 64 shots and 128 receivers. The shots are spaced by 24 m and the receivers are set 12 m apart. This gives an offset of 1536 m.

The first shot of each survey is positioned at the first receiver. Given that the distance between shots is two times the distance between receivers, each shot will have a zero offset trace.

3.6 Modelling scenarios

To allow the wave field to be recorded at various depths through the reservoir, several receiver levels were chosen. For all levels the geometry described in Chapter 3.5.2 is used, except for the depth of the receivers. The twelve depths are given in Table 3.4, and the coverage is shown in Fig. 3.5.

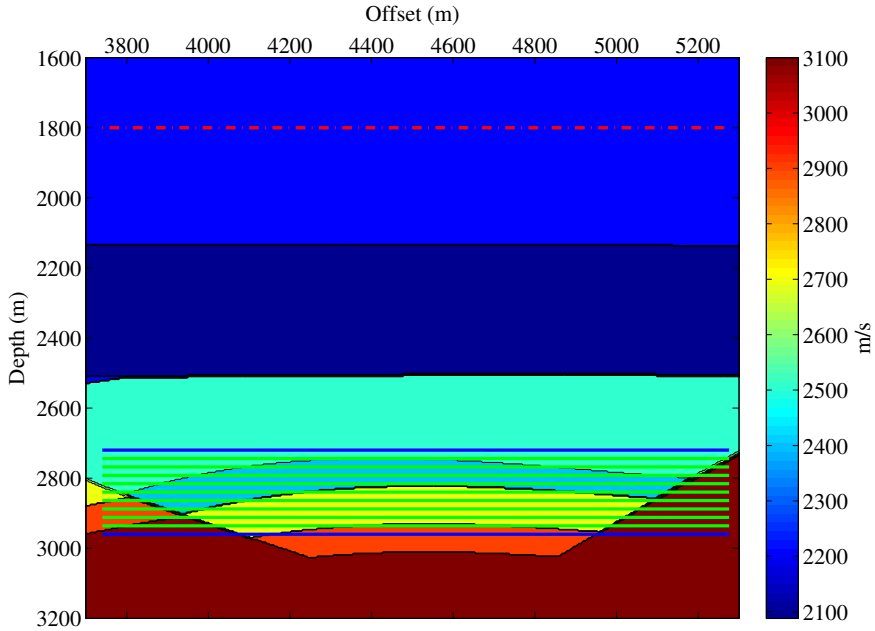

Fig. 3.5: Source level and receiver levels. Dotted line is source level and uppermost recording level.

Table 3.4: Receiver levels.

Scenario	Depth (m)
tm	200 m
tr	1120 m
r0	1144 m
r1	1168 m
r2	1192 m
r3	1216 m
r4	1240 m
r5	1264 m
r6	1288 m
r7	1312 m
r8	1336 m
br	1360 m

Chapter 4
Implementation

In order to explore the methods for time-lapse imaging discussed in Chapter 2.2, they have been implemented in a simple processing workflow (see Appendix C for source code). Since the output from the two methods does not contain the same type of information about changes in the data, the post-processing steps for imaging are quite different and will thus be discussed separately.

The general layout of the workflow is similar for both methods.

1. Initialise geometry and survey parameters.
2. Read data for both surveys.
3. Process input data.
4. Compute desired integral.
5. Process result.
6. Write output.
7. Image result.

Except for the computation of the integral, the main differences are in the way input data are processed before the computation and how the output is processed and imaged after the computation is completed.

For both methods the input data consists of recorded pressure and vertical acceleration fields. Since the actual input is in form of vertical velocity fields they have to be numerically converted to represent particle acceleration, this is described in Appendix B.

To conserve memory and reduce the number of data points involved in the computation, the input data is down-sampled from 0.5 ms to 4 ms. This corresponds to a Nyquist frequency of 125 Hz, which is well within the range of the seismic signal.

Both integrals are computed on a grid by iterating and summing over all shots in the surveys for which they are to be determined. The resulting traces are then kept in a matrix for further processing. In Fig. 4.1 the layout of the resulting matrix is shown. For each point in the matrix, a sum corresponding to the interaction integrals in Eq. (2.34) or (2.67) is evaluated.

		Monitorshot							
		1	**2**	**3**	**4**	**5**	**6**	**7**	**8**
Referenceshot	**1**	$\otimes$	$\times$	$\times$	$\times$	$\times$	$\times$	$\times$	$\times$
	2	$\times$	$\otimes$	$\times$	$\times$	$\times$	$\times$	$\times$	$\times$
	3	$\times$	$\times$	$\otimes$	$\times$	$\times$	$\times$	$\times$	$\times$
	4	$\times$	$\times$	$\times$	$\otimes$	$\times$	$\times$	$\times$	$\times$
	5	$\times$	$\times$	$\times$	$\times$	$\otimes$	$\times$	$\times$	$\times$
	6	$\times$	$\times$	$\times$	$\times$	$\times$	$\otimes$	$\times$	$\times$
	7	$\times$	$\times$	$\times$	$\times$	$\times$	$\times$	$\otimes$	$\times$
	8	$\times$	$\times$	$\times$	$\times$	$\times$	$\times$	$\times$	$\otimes$

Fig. 4.1: Organisation of output matrix from integrals, the circled traces where the shot positions coincide are what is referred to as zero offset in this context.

4.1 Convolution

For the time-convolution type integral given by Eq. (2.34) the summation for each point of the matrix in Fig. 4.1 looks like (ω-dependency omitted)

$$I_{conv}(m,n) = \sum_{i=1}^{i=N} \sum_{j=1}^{j=N} v_3^{(1)}(m,i)p^{(2)}(n,j) - v_3^{(2)})(n,j)p^{(1)}(m,i), \qquad (4.1)$$

where m and i denote shot and receiver numbers for the reference survey, while n and j are shot and receiver numbers of the monitor survey. N is the number of receivers in each survey and assumed to be the same for both surveys. $v_3^{(1),(2)}$ and $p^{(1),(2)}$ are the same properties as defined in Chapter 2.2.

For imaging purposes the result of the time-convolution method is converted to time-space by inverse Fourier transform and imaged as any 2D seismic dataset.

4.2 Correlation

The numerical implementation of the time-correlation interaction integral is done according to the following equation (ω-dependency omitted)

$$I_{corr}(m,n) = \sum_{i=1}^{i=N} \sum_{j=1}^{j=N} [v_3^{(1)}(m,i)]^{\ddagger} p^{(2)}(n,j) + v_3^{(2)})(n,j)[p^{(1)}(m,i)]^{\ddagger}, \quad (4.2)$$

where all parameters are the same as in Eq. (4.1).

With the result of the time-correlation integral imaging is not as straightforward as with the time-convolution variant. There are several methods available to image the data in a meaningful way, but due to a limited time schedule the simplest method has been chosen for this work.

This method involves an inverse Fourier transform to space-time and the subsequent extraction of the zero offset traces. In the end the data is interpolated to a sampling rate of 0.1 ms in order to enhance resolution.

Chapter 5
Results

5.1 Fluid substitution

Table 5.1: Seismic properties of reservoir.

S_w	V_p(m/s)	V_s (m/s)	ρ (kg/m^3)
0.29	2482	1364	2100
0.80	2607	1352	2140
Δ	125	-12	40

To get a time-lapse response from the reservoir, the saturation of water was increased from 0.29 for the reference, to 0.8 for the monitor model by fluid substitution. The changes in seismic properties are given in Table 5.1. They represent a 7% increase in acoustic impedance for the reservoir.

5.2 Seismic modelling

Even though care has been taken to stay within the stability criteria of the finite difference modelling scheme, the synthetic modelling produces certain artifacts in the resulting seismograms. The two most visible are the edge reflections and the grid diffractions as seen in Fig. 5.1. Most of the edge reflections are outside the area of interest and should not present any significant problems. Grid diffractions occur at non-planar interfaces due to the discrete sampling of the input model. Since the reservoir is curved this could lead to unwanted effects in the data analysis.

The time-lapse changes created by fluid substitution produced good time-lapse responses at the reservoir level, as shown in Fig. 5.2. The modelling

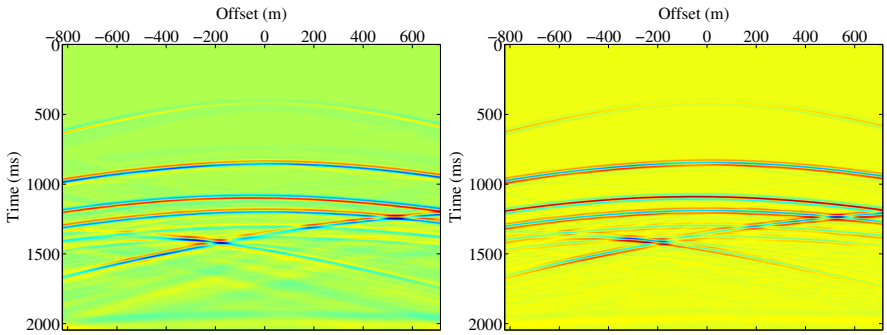

(a) Pressure field. (b) Vertical acceleration field.

Fig. 5.1: Shot gathers of reference survey at 35th shot. The direct wave is removed.

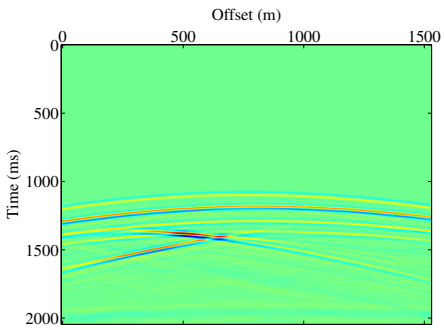

Fig. 5.2: Difference gather calculated from the recorded pressure wave field at the position of the 35th shot.

artifacts and noise above the reservoir are perfectly repeatable, but there are still some non-repeatable artifacts below the reservoir. Since they are of very low amplitude compared to the signal they should have minimal impact on further analysis.

5.3 Convolution

The convolution integral is evaluated and then imaged as a difference wave field at all receiver levels. Since the receiver levels are quite close, 24 m, not all levels are shown.

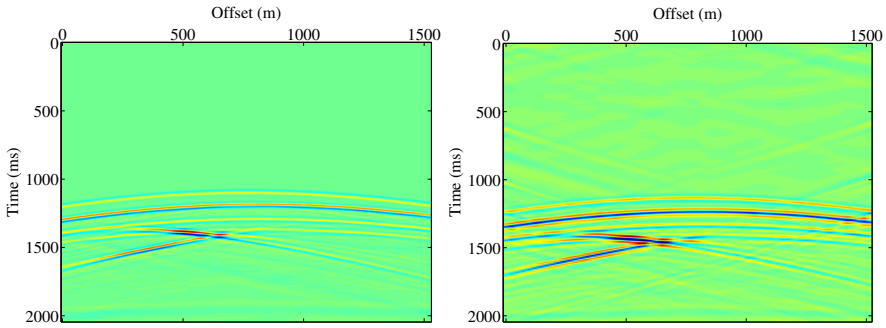

(a) Difference gather for pressure field. (b) Convolution integral.

Fig. 5.3: Difference gather and convolution integral at 35th shot. Receiver level is 200 m, well above the contrast

.

From the theory in Chapter 2.2.3 it is expected that the convolution integral in time-space will resemble the difference gather shown in Fig. 5.2. A comparison of the two is shown in Fig. 5.3.

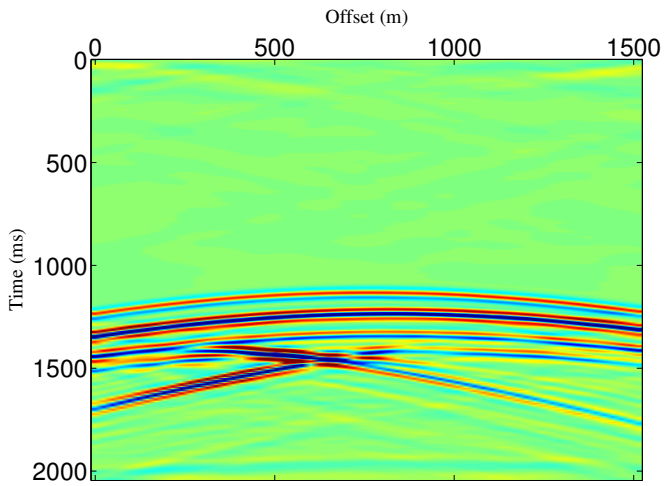

Fig. 5.4: Convolution integral of Eq. (2.34) just above the reservoir (1120 m).

At a level just above the reservoir all the difference reflections are still present. There is also some noise present in the data. This noise is introduced by assuming periodicity when computing the convolution integral. It

is possible to attenuate the noise, but since the data are not to be used in any further analysis this does not serve any purpose.

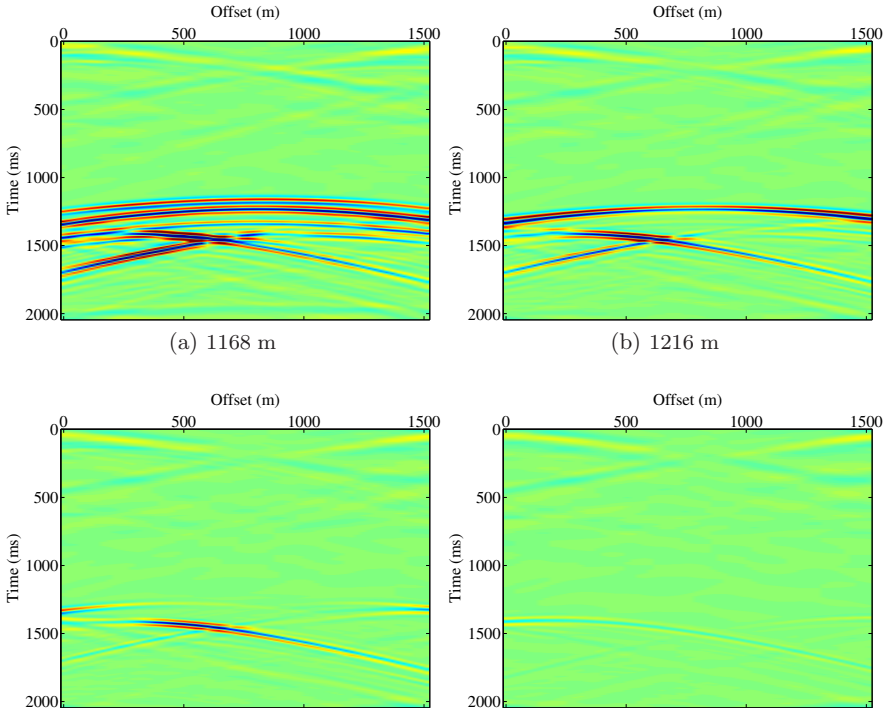

(a) 1168 m (b) 1216 m

(c) 1240 m (d) 1288 m

Fig. 5.5: Convolution integral of Eq. (2.34) at various depths through the reservoir.

While moving the level at which the convolution integral is evaluated down through the reservoir, an increasingly larger portion of the difference reflections disappear. The noise is still present and constant.

Once a level below the contrasting reservoir zone is reached, all difference reflections are removed from the resulting image. There is still some residual noise in the image. A portion of it is attributed to modelling artifacts, while the remainder comes from the convolution integral.

These results give confidence in that the processing scheme prior to evaluation of the convolution integral is correct and that the integral itself is implemented correctly.

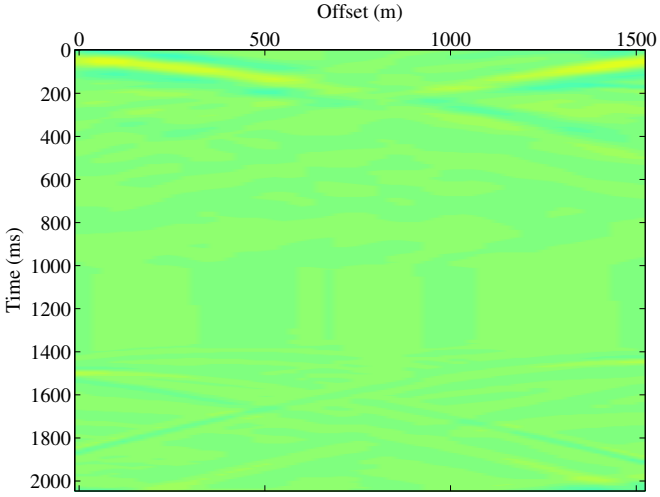

Fig. 5.6: Convolution integral of Eq. (2.34) below reservoir (1360 m).

5.4 Interferometry

Looking at Fig. 5.7a there is some noise present in the computed integral. Most of the noise again appears to be outside the area of interest, and of much lower amplitude than the signal.

The most interesting part of the time-correlation integral is the time-lag of the first peak. In Fig. 5.7, the image is zoomed to show a window of ± 50 ms around zero correlation time-lag. In this figure it is clear that the delay caused by contrasts in the seismic signal changes as the signal moves across the reservoir.

Since the delay observed in the correlation integral relates to velocity changes in the reservoir, this delay should change with the thickness of the reservoir as well. In Fig. 5.8 the delay of the correlation integral relative to the reference survey is plotted together with the shape of the reservoir. The delay from the correlation integral follows the same trends as the approximate change in vertical traveltime. It is also worth noting that the interpolation yields a significant increase in resolution.

The measured changes in traveltime appear to be greatly mispositioned with respect to what is expected from the computed curve. Since the data are not corrected for any travel path effects these will still be present and distort the imaging.

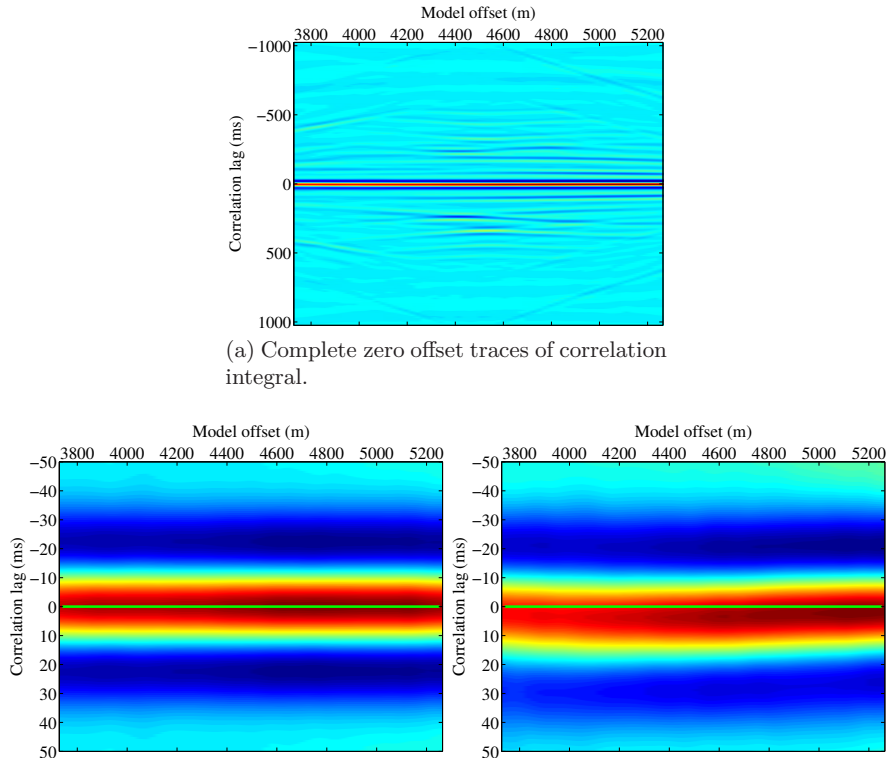

(a) Complete zero offset traces of correlation integral.

(b) Correlation of Reference-Reference.

(c) Correlation of Reference-Monitor.

Fig. 5.7: Zero offset traces of correlation integral in space-time. The green line marks zero correlation lag.

5.4.1 Improving resolution

In an attempt to achieve better definition of the edges of the reservoir, a computational scheme where only limited offset data was attempted. The first attempt was made using a fixed number of five traces to each side of the shot position, to achieve a split-spread configuration. At the edges the split-spread configuration is not an option, so instead the number of traces is reduced. The result of this first attempt is shown in Fig. 5.9a, and has not provided much improvement. Even though a clear definition of the edges is gained, the error in the central part is far too great.

To account for the problems of the central part, a new scheme was implemented. Instead of a fixed number of traces, a minimum number of traces was chosen and a split-spread configuration is enforced wherever possible. This means that at the edges five traces of normal offset data will be included, but towards the central shots an increasing number of traces will be included in a split-spread manner.

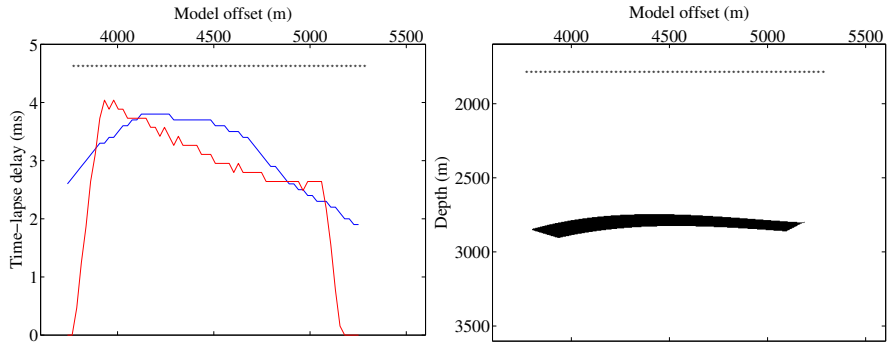

(a) Computed vertical time delay (red) and observed time delay (blue).

(b) Reservoir with shot positions.

Fig. 5.8: Correlation time lag across reservoir and reservoir outline.

Fig. 5.9b shows the results of this adaptive scheme. It has the same increase of delay to the left of the reservoir as observed with the first scheme, but the error in the central parts is drastically reduced in comparison to the first attempt.

In a final attempt to remove the unexpected increase in delay to the left of the reservoir, the adaptive scheme was run with no minimum number of traces. This gives the effect that at the left-most shot, only the zero-offset receiver will be included. As shown in Fig. 5.9c, this did not lead to a significant improvement.

When looking at the results it is clear that this provides a rough scheme to get better definition of the edges of the reservoir, but it does not offer much in the way of overall improved resolution.

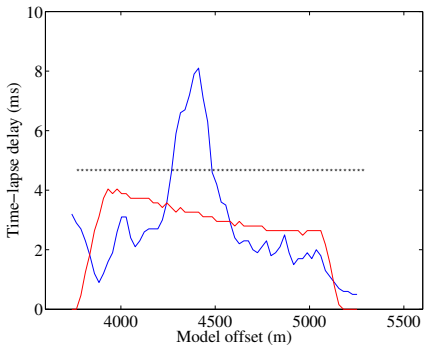

(a) Fixed width of maximum of 11 traces.

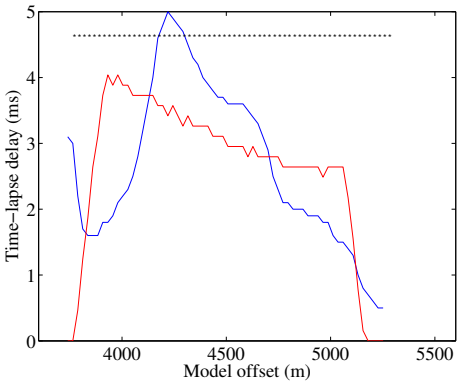

(b) Adaptive width, minimum 4 traces.

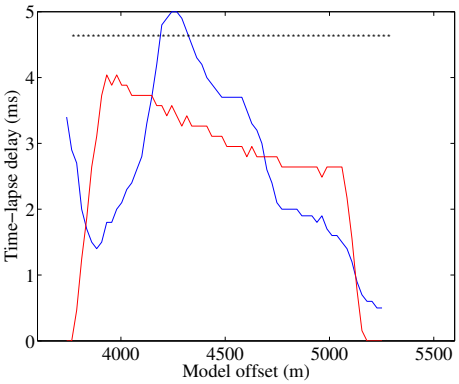

(c) Adaptive width, no minimum.

Fig. 5.9: Correlation time lag using limited offset data.

Chapter 6
Conclusions

An interferometric method for time-lapse imaging using a boundary integral of the time-correlation type has been presented and implemented. In order to test the method and implementation, a synthetic time-lapse dataset was produced using Gassmann fluid substitution and acoustic finite-difference modelling.

A method based on a similar integral, but of the time-convolution type, was also implemented to serve as a way to confirm that the processing scheme was correctly implemented. It is well suited for this application as it is computationally similar to the correlation integral, and produces a difference wave field which is straightforward to image and verify.

The time-convolution integral responds as predicted by the theory. When the imaging level is moved through the region where time-lapse effects are present, difference reflections originating from contrasts above the current level are removed from the resulting image. No quantitative analysis of the result has been performed, but a qualitative evaluation and comparison to conventional difference gathers support the theoretical observations.

For the time-correlation integral the measured time delays correspond well to the predicted trends in vertical traveltime, and the deviation is likely due to lacking correction for travel path differences in the contrast volume, introduced by non-planar interfaces and non-vertical travel paths. The geometry of the reservoir might also introduce some focusing effect, causing the signal to be positioned incorrectly in imaging.

After interpolation of the traces in the correlation integral, resolution beyond the original sampling rate was achieved. This makes it possible to detect changes below the seismic resolution.

Further work on the imaging of both the convolution and correlation integral is needed in order to interpret the results in terms of changes in reservoir properties.

Chapter 7
Discussion

The work presented in this thesis does not fully exploit the potential of the interferometric imaging method. One question which is highly significant if it is ever to be used for "real life" reservoir monitoring, is how to apply it when there are more than one dataset.

Once the method is implemented it can be used to compare any two surveys, with one serving as a reference to the other. However, the reference survey does not necessarily have to represent the initial conditions of the monitored reservoir. In this way it would be possible to examine changes incrementally and also gain information about the rate at which the changes occur. This can in turn be used as input to e.g. fluid flow predictions.

After the attempts to correct for offset effects, it would be interesting to see how well the integral responds to noisy data. The measured increase in the delay outside the left side of the reservoir suggests that some element of noise introduces a false response.

A problem with the scheme applied to reduce the offset effects is that while it to a certain degree will compensate for travel path effect, it also removes data from the correlation, thus leaving the integral less resilient to noise. Some other way of correcting for travel path effects, preferably without reducing input to the correlation, should therefore be found. Although tests could still be performed to see when the lack of data becomes a significant problem. It is clear that a certain amount of traces is needed in order to produce reliable measurements, but how much is enough?

The results also show that the correlation is able to detect changes below seismic resolution. Nothing has been done to explore how sensitive it is at this level of resolution, nor how reliable it is when operating at sub-seismic resolutions.

Chapter 8
Recommendations

More work should be done on imaging and inversion of the convolution integral. Of the two integrals, it is the simplest to interpret, and relates to physical phenomena in terms of true difference reflections. The first step would be to remove the travel path effects and position the difference reflections correctly in the subsurface.

Additional processing steps to properly image the correlation integral should also be tested. Application of the Radon transform would enable imaging of the phase changes of plane waves with a defined angle of incidence. An inversion scheme to relate the measured traveltime changes to velocity changes, and further to saturation changes should also be explored.

A back-scattering of the wave field should also be performed to test the correlation integral at depths within the contrast domain. Following the promising behaviour of the convolution integral, this could lead to interesting results.

References

L. Amundsen, B. Arntsen, J. Helgesen, K. Hokstad, M. Landrø, R. Mittet, and R. Sollie. *SDI Documentation*. IKU, 1997. Internal documentation.

P. Avseth, T. Mukerji, and G. Mavko. *Quantitative seismic interpretation: applying rock physics tools to reduce interpretation risk*. Cambridge University Press, Cambridge, 2005. ISBN 0-521-81601-7.

J. G. Berryman. Origin of Gassmann's equations. *Geophysics*, 64(5):1627–1629, 1999.

J. P. Castagna, M. L. Batzle, and R. L. Eastwood. Relationships between compressional-wave and shear-wave velocities in clastic silicate rocks. *Geophysics*, 50(4):571–581, 1985.

M. W. P. Dillen. *Time-lapse seismic monitoring of subsurface stress dynamics*. PhD thesis, Delft University of Technology, 2000.

M. W. P. Dillen, J. T. Fokkema, and C. P. A. Wapenaar. Recursive elimination of temporal contrasts between time-lapse acoustic wave fields. *Journal of Seismic Exploration*, 11:41–57, 2002.

J. T. Fokkema and P. M. van den Berg. *Seismic Applications of Acoustic Reciprocity*. Elsevier Science Publishers B.V., 1993.

M. Frigo and S. G. Johnson. The design and implementation of FFTW3. *Proceedings of the IEEE*, 93(2):216–231, 2005. special issue on "Program Generation, Optimization, and Platform Adaptation".

F. Gassmann. Elastic waves through a packing of spheres. *Geophysics*, 16(4):673–685, 1951.

O. Holberg. Computational aspects of the choice of operator and sampling interval for numerical differentiation in large-scale simulation of wave phenomena. *Geophysical Prospecting*, 35(6):629–655, 1987. doi: 10.1111/j.1365-2478.1987.tb00841.x.

K. R. Kelly, R. W. Ward, S. Treitel, and R. M. Alford. Synthetic seismograms: A finite -difference approach. *Geophysics*, 41(1):2–27, 1976.

E. Kreyszig. *Advanced Engineering Mathematics*. John Wiley & Sons, Inc, 8th edition, 1999.

Ø. Kvam. *Pore pressure estimation from single and repeated seismic data sets*. PhD thesis, NTNU, Trondheim, 2005. Avhandling (dr. ing.) – Norges Teknisk-Naturvitenskapelige Universitet, 2005.

Ø. Kvam and M. Landrø. Pore-pressure detection sensitivities tested with time-lapse seismic data. *Geophysics*, 70(6):O39–O50, 2005.

M. Landrø. Repeatability issues of 3-d VSP data. *Geophysics*, 64(6):1673–1679, 1999. doi: 10.1190/1.1444671.

M. Landro, O. A. Solheim, E. Hilde, B. O. Ekren, and L. K. Stronen. The Gullfaks 4D seismic study. *Petroleum Geoscience*, 5(3):213–226(14), aug 1999.

MathWorks. *MatLab 7 – Function Reference: Volume 2 (F-O)*. The MathWorks, Inc, 2006b edition, Sept. 2006.

G. Mavkov, T. Mukerji, and J. Dvorkin. *The Rock Physics Handbook*. Cambridge University Press, 1998.

W. H. Press, S. A. Teukolsky, W. T. Vetterling, and B. P. Flannery. *Numerical Recipes in FORTRAN*. Cambridge University Press, 2nd edition, 1992.

T. M. Smith, C. H. Sondergeld, and C. S. Rai. Gassmann fluid substitutions: A tutorial. *Geophysics*, 68(2):430–440, 2003.

A. Stovas and M. Landrø. Optimal use of PP and PS time-lapse stacks for fluid-pressure discrimination. *Geophysical Prospecting*, 52(4):301–312, 2004. doi: 10.1111/j.1365-2478.2004.00420.x.

A. Stovas, M. Landrø, and B. Arntsen. A sensitivity study based on 2D synthetic data from the Gullfaks Field, using PP and PS time-lapse stacks for fluid-pressure discrimination. *Journal of Geophysics and Engineering*, 3(4):314–328, 2006.

A. J. Wild and S. C. Singh. Some unintended features of elastic finite-difference models. *Geophysical Prospecting*, 46(1):79–101, 1998. doi: 10.1046/j.1365-2478.1998.810316.x.

Appendix A
The Fast Fourier Transform

The fast Fourier transform (FFT) is an efficient algorithm for computing the forward and inverse discrete Fourier transform in a computer.

Given $x_0, \ldots, x_{N-1}$ as complex numbers, the DFT is defined as follows (Press et al., 1992)

$$X_k = \sum_{n=0}^{N-1} x_n \mathrm{e}^{\frac{2\pi \mathrm{i}}{N} nk} \qquad k = 0, \ldots, N-1, \tag{A.1}$$

The non-normalised inverse transform is obtained by changing the sign of the exponent.

Implementing Eq. A.1 as-is would yield an inefficient and computationally intensive solution using $\mathcal{O}(N^2)$ arithmetic operations, while the FFT algorithms will reduce this number to $\mathcal{O}(N \log N)$ (Press et al., 1992).

A.1 Implementation in MatLab

MatLab uses an implementation of the fast Fourier transform provided by the free FFTW[1] library developed at MIT (MathWorks, 2006).

Since arrays in MatLab are 1-indexed, Eq. A.1 is modified, leading to the following for the forward and inverse transforms respectively

[1] Fastest Fourier Transform in the West

$$X(k) = \sum_{j=1}^{N} x(j)\omega_N^{(j-1)(k-1)} \tag{A.2}$$

$$x(j) = \frac{1}{N}\sum_{k=1}^{N} X(k)\omega_N^{-(j-1)(k-1)} \tag{A.3}$$

$$\omega = \mathrm{e}^{-\frac{2\pi i}{N}} \tag{A.4}$$

From Eq. (A.3) it can be seen that MatLab normalises the inverse transform by $\frac{1}{N}$.

The output from the MatLab functions is ordered such that the positive frequencies are in the first half of the output and the negative frequencies in the second half. The consequence of this is that

$$X(\frac{N}{2} + k) = X^{\ddagger}(k). \tag{A.5}$$

This is a property of the output from the library MatLab uses to compute the FFT (Frigo and Johnson, 2005).

A.2 Integration

Being no more than a faster way of computing a DFT, the FFT has the same mathematical properties. The properties of importance for this work are those with respect to convolution, cross-correlation and integration.

For the continuous Fourier transform an integral in the time-domain will be transformed as (Kreyszig, 1999)

$$\mathcal{F}\left\{\int x(t)dt\right\} = \frac{1}{i\omega}\hat{x}(\omega) \tag{A.6}$$

When applied to the fast Fourier transform this expression takes on a different form. In case of the implementation used by MatLab it will appear as

$$\frac{1}{1 - e^{-ik\frac{2\pi}{N}}}\hat{f}(k) \tag{A.7}$$

Appendix B
Modelling output conversion

Since the modelling software used outputs the pressure field and particle acceleration in the vertical direction, while the interaction quantities are defined by pressure and particle velocity (Eq. 2.21) it is necessary to perform a conversion from particle acceleration to velocity.

The conversion is performed by applying the relationship

$$a(x,t) = \frac{\partial v(x,t)}{\partial t} \tag{B.1}$$

which implies that the velocity can be expressed as

$$v(x,t) = \int_{t=0}^{T} a(x,t)\partial t \tag{B.2}$$

Implementing this approach directly in a numerical workflow would be impractical. Since the datasets are transformed to the Fourier-domain for calculation of the interaction integrals, the integral property of the Fourier transform can be exploited. This leads to the following relationship

$$\hat{v}(x,\omega) = \frac{1}{\mathrm{i}\omega}\hat{a}(x,\omega) \tag{B.3}$$

As discussed in Appendix A.2 equation B.3 does not hold as-is for the FFT and must be modified according to Eq. (A.7), giving the following expression for the conversion from particle acceleration to velocity

$$\hat{v}(x,\omega_k) = \frac{1}{1-e^{-ik\frac{2\pi}{N}}}\hat{a}(x,\omega_k) \tag{B.4}$$

In the actual implementation this relationship is only computed up to $\frac{N}{2}$, since the other half of the signal can be reconstructed using the symmetry of the FFT according to Eq. (A.5).

Appendix C
MatLab source code

C.1 Model calibration

Listing C.1: Model calibration

```
function [VP,VS,RHO] = calibratemodel(vp,vs,rho,res,
    zonef,hcf,wf)
% Initialize output
VP = vp;
VS = vs;
RHO = rho;

% Read parameters
[khc,rhohc,volhc] = fluid(hcf);
[kw,rhow] = fluid(wf);
[sw,kfr,kma,g,rhoma,por] = resdata(zonef);

% Calculate fluid and bulk density from reservoir
    parameters
rhopfl = mean(sw)*rhow + (1-mean(sw))*sum(rhohc.*volhc)
rhob = (1-mean(por))*mean(rhoma) + mean(por)*rhopfl
% Calculate fluid bulk modulus
v = mean(sw)*kw+(1-mean(sw))*sum(khc.*volhc);
r = 1/((mean(sw)/kw)+(1-mean(sw))*sum(volhc./khc));
kpfl = .5*(v+r);

RHO(res) = rhob;

% Calculate velocities from reservoir parameters
VS(res) = sqrt(mean(g)/rhob);
M = mean(kfr) + (4/3)*mean(g) + ( (mean(kfr)-mean(kma)
    )*( mean(kfr)-mean(kma) ) )/( mean(kma) * (1 - mean(
```

```
    por) + mean(por)*(mean(kma)/kpfl) - mean(kfr)/mean(
    kma) ) );
VP(res) = sqrt(M/rhob);
end
```

C.2 Fluid substitution

Listing C.2: Fluid substitution

```
function [vpsat,vssat,rhosat,Ksat,Gsat] = flsubs(vp,vs,
    rho,res,fldata,reszones)
% FLSUBS - Perform fluid substitution
%

vpsq = vp.*vp;
vssq = vs.*vs;

% Initial moduli
Kin = rho.*(vpsq-(4/3)*vssq);
Gin = rho.*vssq;

% Initialize output
Ksat = Kin;
Gsat = Gin;
vpsat = vp;
vssat = vs;
rhosat = rho;

% Read parameters
[hc.k,hc.rho,hc.s] = fluid('fldata.in');
[w.k,w.rho] = fluid('wdata.in');
[w.s,kfr,kma,g,rhoma,por] = resdata('reszones.in');

% Calculate fluid properties
[rhopfl, kpfl] = mixfluid(w, hc);
% Calculate bulk density
rhob = (1-mean(por))*mean(rhoma) + mean(por)*rhopfl;

rhosat(res) = rhob;

%mean(Gin(res))
%mean(g)
%sqrt(mean(g)/rhob)
```

```
%rhob * mean(vpsq(res))
%M = mean(kfr) + (4/3)*g + ( (mean(kfr)-mean(kma) )*(
    mean(kfr)-mean(kma) ) )/( mean(kma) * (1 - mean(por)
     + mean(por)*(mean(kma)/kpfl) - mean(kfr)/mean(kma)
    ) );
%sqrt(M/rhob)

Ksat(res) = gassmann(mean(kfr), mean(kma), kpfl, mean(
    por));
vpsat(res) = sqrt((Ksat(res) + (4/3)*Gsat(res))./rhosat
    (res));
vssat(res) = sqrt(g/rhob);
%mean(vpsat(res))
end
```

Listing C.3: Implementation of the Gassmann equation

```
function Ksat = gassmann(Kfr, Kma, Kfl, por)
% GASSMANN   Perform fluid substitution using Gassmann'
    s relation
%   Usage: Ksat = gassmann(Kfr, Kma, Kfl, por)
%
%   Arguments (in order):
%    - Kfr: Rock framework bulk modulus
%    - Kma: Mineral matrix bulk modulus
%    - Kfl: Fluid bulk modulus
%    - por: Porosity
%
%   The saturated bulk modulus is returned.
a = (1-(Kfr./Kma)).*(1-(Kfr./Kma));
b = (por./Kfl) + ((1-por)./Kma) - (Kfr./(Kma.*Kma));

Ksat = Kfr + a./b;
end
```

Listing C.4: Mix fluid components

```
function [rhofl, kfl] = mixfluid(water, hc)
    sw = water.s;
    rhow = water.rho;
    kw = water.k;
    volhc = hc.s;
    rhohc = hc.rho;
    khc = hc.k;

```

```
    rhofl = mean(sw)*rhow + (1-mean(sw))*sum(rhohc.*
        volhc);
    v = mean(sw)*kw+(1-mean(sw))*sum(khc.*volhc);
    r = 1/((mean(sw)/kw)+(1-mean(sw))*sum(volhc./khc));
    kfl = .5*(v+r);
end
```

C.3 Acceleration to velocity

Listing C.5: Convert particle acceleration to particle velocity

```
function velocity = a2v_xf(a)
for i=1:size(a,2)
    f = a(1:size(a,1)/2+1,i);
    v = intfft(f,size(a(:,i),1));
    v = flipfft(v);
    velocity(:,i) = v;
end
end
```

Listing C.6: Integration in the Fourier domain

```
function integral = intfft(fft, N)
integral = zeros(size(fft));
for k=1:N/2+1
    integral(k,:) = (1 / (1 - exp(-j*k*(2*pi/N)))) .*
        fft(k,:);
end
end
```

C.4 Interaction integrals

Listing C.7: time-convolution type

```
%% Parameters
nshot = 64;
nrec = 128;
nt = 4096;
dt = 0.0005;
dshot = 24;
```

```
nsamp = 8;
%recpos = 'tm';
refshot = 35;

%% pre-allocate arrays for speed
ref_p_tx = zeros(nt/nsamp,nrec,nshot);
ref_a_tx = zeros(nt/nsamp,nrec,nshot);
mon_p_tx = zeros(nt/nsamp,nrec,nshot);
mon_a_tx = zeros(nt/nsamp,nrec,nshot);

conv_fx = zeros(nt/nsamp,nshot,nshot);

%% Read all reference data
[ref_a_tx, ref_p_tx] = readsdidata('base',recpos,nshot,
    nrec,nt,nsamp);

%% Read all monitor data
[mon_a_tx, mon_p_tx] = readsdidata('s80',recpos,nshot,
    nrec,nt,nsamp);

%% Do stuff for all shots in monitor survey
for ref=1:nshot
    ref_p_fx = fft(ref_p_tx(:,:,ref));
    ref_a_fx = fft(ref_a_tx(:,:,ref));
    ref_v_fx = a2v_xf(ref_a_fx);

    for mon=1:nshot
        disp(sprintf('Processing reference %03d and
            monitor %03d of %03dx%03d ... %03d left',ref
            ,mon,nshot,nshot,(nshot*nshot)-(mon+nshot*(
            ref-1))));
        mon_p_fx = fft(mon_p_tx(:,:,mon));
        mon_a_fx = fft(mon_a_tx(:,:,mon));
        mon_v_fx = a2v_xf(mon_a_fx);

        conv_fx(:,mon,ref) = sum(ref_v_fx.*mon_p_fx -
            ref_p_fx.*mon_v_fx, 2);
    end
end

%% cleanup
clear ref_v_fx ref_a_fx ref_p_fx mon_v_fx mon_p_fx
    mon_a_fx mon_v_fx;
clear i j n nfft ref mon;
```

```
%% Dump reference shot to file
fid = fopen(strcat('convint_',recpos,'_',num2str(
    refshot),'_tx.bin'), 'w', 'l');
fwrite(fid, real(ifft(conv_fx(:,:,refshot))), 'float32'
    );
fclose(fid);
clear fid;

%% Save reference shot for later use
eval(['convint_',recpos,'_',num2str(refshot),'_fx␣=␣
    conv_fx(:,:,refshot);']);

%% Dump integrals to file
writecomplex3d(strcat('convint_',recpos,'_fx.bin'),
    conv_fx);

%% Clean out everything (almost)
clear conv_fx
```

Listing C.8: time-correlation type

```
%% Parameters
nshot = 64;
nrec = 128;
nt = 4096;
dt = 0.0005;
dshot = 24;
nsamp = 8;
recpos = 'tm';
refshot = 35;

%nyquist = 1/(2*dt*nsamp);

%f = [(0:nt/(nsamp*2)) -(nt/(nsamp*2)-1:-1:1)]/(dt*nt);
%omega = f*2*pi;

%% pre-allocate arrays for speed
ref_p_tx = zeros(nt/nsamp,nrec,nshot);
ref_a_tx = zeros(nt/nsamp,nrec,nshot);
mon_p_tx = zeros(nt/nsamp,nrec,nshot);
mon_a_tx = zeros(nt/nsamp,nrec,nshot);
dir_p_tx = zeros(nt/nsamp,nrec,nshot);
dir_a_tx = zeros(nt/nsamp,nrec,nshot);

%% Read all reference data
```

```
[ref_a_tx, ref_p_tx] = readsdidata('base',recpos,nshot,
    nrec,nt,nsamp);

%% Read all monitor data
[mon_a_tx, mon_p_tx] = readsdidata('s80',recpos,nshot,
    nrec,nt,nsamp);

%% Read direct wave
[dir_a_tx, dir_p_tx] = readsdidata('direct',recpos,
    nshot,nrec,nt,nsamp);

%% Compute scattered wave fields
ref_p_sct_tx = ref_p_tx-dir_p_tx;
ref_a_sct_tx = ref_a_tx-dir_a_tx;
mon_p_sct_tx w= mon_p_tx-dir_p_tx;
mon_a_sct_tx = mon_a_tx-dir_a_tx;

%% Clean out full wave fields
clear dir_a_tx dir_p_tx mon_a_tx mon_p_tx ref_a_tx
    ref_p_tx;

%% pre-allocate working arrays
ref_p_fx = complex(zeros(nt/nsamp,nrec));
ref_a_fx = complex(zeros(nt/nsamp,nrec));
ref_v_fx = complex(zeros(nt/nsamp,nrec));
mon_p_fx = complex(zeros(nt/nsamp,nrec));
mon_a_fx = complex(zeros(nt/nsamp,nrec));
mon_v_fx = complex(zeros(nt/nsamp,nrec));

corr_fx = complex(zeros(nt/nsamp,nshot,nshot));

%% Do the integral
for ref=1:nshot
    ref_p_fx = fft(ref_p_sct_tx(:,:,ref));
    ref_a_fx = fft(ref_a_sct_tx(:,:,ref));
    ref_v_fx = a2v_xf(ref_a_fx);

    for mon=1:nshot
        disp(sprintf('Processing reference %03d and
            monitor %03d of %03dx%03d ... %03d left',ref
            ,mon,nshot,nshot,(nshot*nshot)-(mon+nshot*(
            ref-1))));
        mon_p_fx = fft(mon_p_sct_tx(:,:,mon));
        mon_a_fx = fft(mon_a_sct_tx(:,:,mon));
        mon_v_fx = a2v_xf(mon_a_fx);
```

```
        corr_fx(:,mon,ref) = sum(ref_p_fx.*conj(mon_v_fx) + ref_v_fx.*conj(mon_p_fx), 2);
    end
end

%% cleanup
clear ref_v_fx ref_a_fx ref_p_fx mon_v_fx mon_p_fx mon_a_fx mon_v_fx;
clear i j n nfft ref mon;

%% extract diagonal (zero offset integrals)
diag = zeros(nt/nsamp,nshot);
for i=1:nshot
    diag(:,i) = corr_fx(:,i,i);
end
eval(['corrint_',recpos,'_diag_fx = diag;']);
clear diag i;

%% Dump output to file
writecomplex3d(strcat('corrint_',recpos,'_fx.bin'), corr_fx);

%% Clean out everything (almost)
clear corr_fx ref_p_sct_tx ref_a_sct_tx mon_p_sct_tx mon_a_sct_tx
```